Journal of Rock Mechanics and Geotechnical Engineering 16 (2024) 4815–4834

Contents lists available at ScienceDirect

Journal of Rock Mechanics and Geotechnical Engineering

journal homepage: www.jrmge.cn

Full Length Article

Anisotropic characteristics and creep model for thin-layered rock under true triaxial compression

Tianxiang Song [a, b], Xia-Ting Feng [a, b, *], Yangyi Zhou [a, b], Chengxiang Yang [a, b], Xiaojun Yu [a, b]

[a] Key Laboratory of Ministry of Education on Safe Mining of Deep Metal Mines, School of Resources and Civil Engineering, Northeastern University, Shenyang, 110819, China
[b] Key Laboratory of Liaoning Province on Deep Engineering and Intelligent Technology, Northeastern University, Shenyang, 110819, China

ARTICLE INFO

Article history:
Received 13 September 2023
Received in revised form
17 January 2024
Accepted 29 February 2024
Available online 20 May 2024

Keywords:
Inherent anisotropic rock
Creep failure
True triaxial compression
Three-dimensional creep model

ABSTRACT

The failure phenomenon of thin-layered rock tunnels not only exhibits asymmetric spatial characteristics, but also significant time-dependent characteristics under high in-situ stress, which is attributed to the time-dependent fracture of thin-layered rocks. This paper conducted a series of true triaxial creep compression tests on typical thin-layered rock siliceous slate with acoustic emission technique to reveal its anisotropic time-dependent fracture characteristics. The anisotropic long-term strength, creep fracturing process, and fracture orientation characteristics of thin-layered rocks under different loading angles (β, ω) and intermediate principal stress were summarized. A three-dimensional (3D) non-linear visco-plastic creep model for thin-layered rock was developed to simulate its anisotropic creep behavior. The time-dependent fracturing of rocks during true triaxial creep loading is reflected through the change of equivalent strain based on an improved Euler iteration method. By constructing the plastic potential function and overstress index related to loading angles and stress state, the anisotropic time-dependent fracturing process and propagation of thin-layered rocks under different loading angles and intermediate principal stress are expounded. The model was validated experimentally to show it can reflect the long-term strength and creep deformation characteristics of thin-layered rocks under true triaxial compression.
© 2024 Institute of Rock and Soil Mechanics, Chinese Academy of Sciences. Published by Elsevier B.V. This is an open access article under the CC BY-NC-ND license (http://creativecommons.org/licenses/by-nc-nd/4.0/).

1. Introduction

In deep rock engineering, rock mass is under the condition of unequal high stress in three principal directions ($\sigma_1 > \sigma_2 > \sigma_3$) after excavation, and the failure of thin-layered rock mass (rock stratum thickness <0.1 m) can be jointly controlled by high in-situ stress, bedding structure and the direction of tunnel axis (Zhou et al., 2016; Ismael et al., 2019; Liu et al., 2022, 2023). Moreover, the failure of thin-layered rock tunnels has obvious time-dependent characteristics. For example, due to the anisotropy of carbonaceous slate and siliceous slate and high in situ stress, Muzhailing tunnel and Haibaluo tunnel in China experienced severe asymmetric large deformation, and the deformation continued to develop after 90 and 30 days of excavation, respectively (Liu et al., 2005; Guo et al., 2019). Therefore, studying the anisotropic time-dependent failure mechanism of thin-layered rock under true triaxial stress, and establishing an appropriate three-dimensional (3D) time-dependent mechanical model to simulate its anisotropic failure behavior, helps us understand the evolution of thin-layered rock mass disasters and provide a scientific basis for supporting methods. The loading angle pair (β and ω) needs to be defined before true triaxial compression tests (Mogi, 2006). Herein, β is defined as the angle between bedding plane and the direction of maximum principal stress, ω is defined as the angle between bedding plane strike and the direction of intermediate principal stress (Fig. 1).

Many researchers have studied the strength, deformation and

* Corresponding author. Key Laboratory of Ministry of Education on Safe Mining of Deep Metal Mines, School of Resources and Civil Engineering, Northeastern University, Shenyang, 110819, China.
E-mail address: fengxiating@mail.neu.edu.cn (X.-T. Feng).
Peer review under responsibility of Institute of Rock and Soil Mechanics, Chinese Academy of Sciences.

https://doi.org/10.1016/j.jrmge.2024.02.018
1674-7755/© 2024 Institute of Rock and Soil Mechanics, Chinese Academy of Sciences. Published by Elsevier B.V. This is an open access article under the CC BY-NC-ND license (http://creativecommons.org/licenses/by-nc-nd/4.0/).

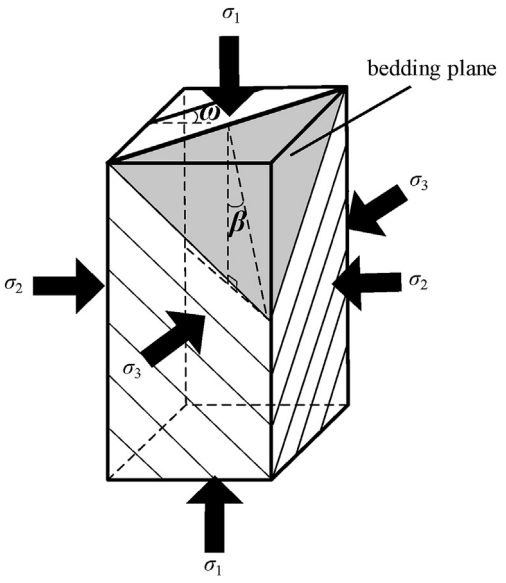


Fig. 1. Definition of true triaxial loading angles for thin-layered rock samples (modified after Mogi, 2006).

failure characteristics of thin-layered rocks based on Brazilian splitting tests, uniaxial, conventional triaxial and true triaxial compression tests, etc. (Zhang et al., 2011; Ismael et al., 2014; Deng et al., 2018; Xu et al., 2018a, b; Liu et al., 2020, 2022, 2023), and established several failure criteria and mechanical models for anisotropic rock (Ismael et al., 2015, 2017, 2019; Liu et al., 2023). These studies are of significance for understanding the instantaneous mechanical properties of thin-layered rocks, however, the anisotropic long-term strength and time-dependent failure mechanism of thin-layered rocks remain to be investigated. In the study of creep properties of thin-layered rocks, most researchers have studied the influence of angle β on the creep properties of thin-layered rocks based on uniaxial or conventional triaxial creep tests. For example, some researchers (Sone and Zoback, 2014; Liu et al., 2015; Rassouli and Zoback, 2018) found that the total deformation of thin-layered rock with $\beta = 90°$ is greater than that with $\beta = 0°$; Xu et al. (2020) found that the creep strength and failure strain of phyllite are both maximized at $\beta = 90°$, followed by $\beta = 0°$, and minimized at $\beta = 30°$. However, to understand the creep properties of thin-layered rocks in deep engineering situations, it is also necessary to consider the influences of angle ω and intermediate principal stress. Moreover, existing research mostly focuses on the creep deformation and strength characteristics of thin-layered rocks, with little attention paid to the time-dependent fracture evolution process of thin-layered rocks during creep process, which is not conducive to understanding the failure mechanism of rock masses.

There are many studies on creep models of homogeneous rocks in the literature, including empirical models, improved rheological element models based on fractional order theory and damage theory (Zhou et al., 2011; Zhao et al., 2018; Yan et al., 2020), models based on Perzyna's overstress theory (Huang et al., 2022), etc., but there are few models that consider the influence of bedding planes on the creep behavior of thin-layered rocks. The creep failure characteristics of thin-layered rocks under different loading angles and intermediate principal stress show significant anisotropy. Establishing an appropriate 3D creep model to simulate the anisotropic fracturing process and fracture orientation of thin-layered rocks at different stress levels and loading angles is a necessary step in studying the long-term stability of thin-layered rock masses in deep engineering operations. In terms of creep models for layered rocks, some researchers based on different theories and methods described the creep behavior of transversely isotropic rocks, such as microstructure tensor and homogenization methods (Pietruszczak et al., 2004; Choo et al., 2021), rheological element theory (Xu et al., 2019), fractional order theory (Kou et al., 2023), visco-plasticity theory (Wang et al., 2018), and crack tensor analysis (Tian et al., 2021). However, most existing creep models are based on uniaxial or conventional triaxial creep tests, which are unable to provide a basis for establishing a suitable 3D creep model for thin-layered rocks (Ismael and Konietzky, 2017). These models are often one-dimensional or two-dimensional and cannot accurately reflect the creep characteristics of thin-layered rocks under true triaxial compression of Ismael and Konietzky (2019). The strain-rate function in these models usually uses time as a variable, which is contrary to the principle of frame indifference for formulation of a constitutive model and the dimensions on each side of the formulae are often inconsistent.

In view of this, the anisotropic long-term strength, creep deformation, and fracture characteristics of a thin-layered siliceous slate under different loading angles and stress states were investigated based on true triaxial creep compression tests and assisted by acoustic emission (AE) monitoring. Then, based on the experimental results, a 3D creep model for thin-layered rock was constructed, and the model was validated by the true triaxial creep test results of siliceous slate.

2. Materials and methods

2.1. Physical properties of siliceous slate

Siliceous slate is a typical thin-layered metamorphic rock. A true triaxial compression sample and thin-section identification results of siliceous slate are shown in Fig. 2. From the thin-section identification results, it can be seen that the bedding planes are formed due to the directional arrangement of siliceous minerals and

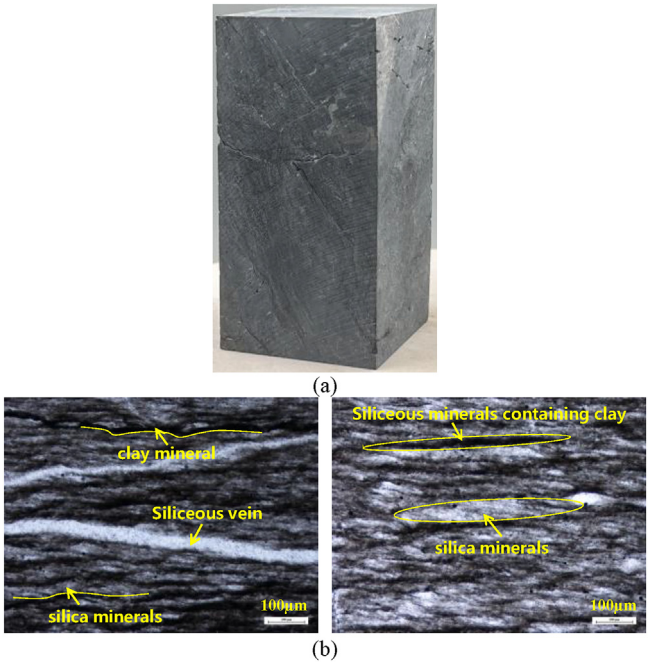


Fig. 2. (a) True triaxial sample of siliceous slate, and (b) Thin-section photographs of siliceous slate.

siliceous minerals containing clay, and the bonding force between bedding planes is weak, which is the primary reason for the anisotropy of siliceous slate. Siliceous slate can be classified as a type of rock material that is very complex at the microscopic scale and has a layered structure at a macroscopic scale.

The X-ray diffraction spectra of siliceous slate are shown in Fig. 3 and Table 1. The horizontal axis in Fig. 3 represents the diffraction angle, and different minerals will produce protrusions at different positions. The area of the peaks represents the relative content of the mineral. The results indicate that this rock is mainly composed of quartz with a small amount of clay minerals and calcite.

2.2. Test scheme and test apparatus

The creep properties of thin-layered rocks under true triaxial stress conditions are influenced by various factors, and there are many combinations of experimental conditions. It is impossible (and indeed unnecessary) to conduct experiments under all conditions. For deep tunnel engineering, stress concentration occurs in the tangential direction and stress release occurs in the radial direction after tunnel excavation, while axial stress changes little. Therefore, after tunnel excavation, the stress on the surrounding rock in the tangential direction is much greater than the other two directions (σ_1 is much greater than σ_2 and σ_3). The failure of tunnel surrounding rock is often caused by tangential stress concentration. This study primarily focuses on the engineering field, the intermediate principal stress level in the experiment is therefore relatively low (the stress state parameter $b = (\sigma_2\text{-}\sigma_3)/(\sigma_1\text{-}\sigma_3) < 0.5$). Therefore, several typical conditions were selected for testing, which can reflect the general characteristics in the creep properties of thin-layered rocks under different intermediate principal stress and loading angles, the test scheme is shown in Table 2. The specimens measured 40 mm × 40 mm × 80 mm (Fig. 2a).

True triaxial creep compression tests were performed on a rigid true triaxial apparatus for analyzing deformation and failure features of deep weak rock under excavation stress paths, which was designed and developed by Northeastern University in Shenyang, Liaoning Province, China, as shown in Fig. 4 (Feng et al., 2023). The loading mode of the equipment is rigid loading in all three principal loading directions, as shown in Fig. 4b. The sample was placed in the linked interlocking clamp before test to avoid the stress gap caused by dilation of the specimen under load (Fig. 5). To capture the deformation of rock in the true triaxial test, six grating displacement extensometers with a range of 10–20 mm were used to monitor the deformation in three principal stress directions

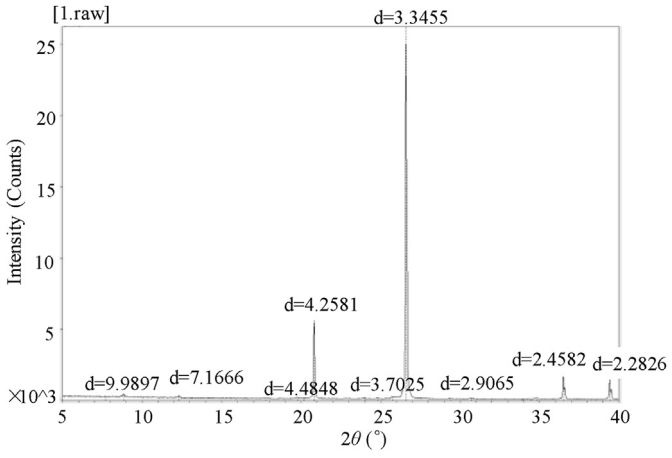


Fig. 3. X-ray diffraction pattern of siliceous slate.

Table 1
X-ray diffraction analysis result of siliceous slate.

Rock composition	Quartz	Calcite	Clay minerals	Ankerite
Content (%)	91.9	1	5.7	1.4

independently. A true triaxial creep compression test was conducted using a stepwise loading method. Fig. 6 shows the specific loading stages used in the true triaxial creep compression test at $\beta = \omega = 0°$. The loading rate is 2.5 MPa/min to meet the requirements of static loading conditions (Liang et al., 2012). When the deformation rate in the main expansion direction (σ_2 or σ_3 direction) is less than 0.001 mm/h and the creep loading time is greater than 10 h, it is considered that the sample has entered a stable creep stage and the next stage of loading can be proceeded.

The PCI-2 AE monitoring system produced by the American Physical Acoustics Company was used for the acquisition of AE signals. The threshold, pre-amplification, sampling frequency, and sampling length were set to 35 dB, 40 dB, 2 MHz, and 2 k, respectively. During the experiment, ten Nano30 sensors were adopted to acquire AE signals, for which the frequency response range was 125–750 kHz. Each sensor was equipped with a 2/4/6-AST preamplifier, and the sensors were placed within the linked interlocking clamp, as shown in Fig. 5. To guarantee good reception of the AE signals by the sensors, the interfaces among the specimen, the waveguide blocks and sensors were smeared with Vaseline™ for coupling.

3. Test results and analysis

3.1. Long-term strength, deformation, and failure characteristics of siliceous slate

The long-term strength values of siliceous slate under different loading angles and intermediate principal stress are shown in Fig. 7. The long-term strength was determined by using the rheological volumetric strain inflection point method. In Fig. 7, except for samples at $\beta = 75°$, which exhibit significant discreteness, the long-term strength of siliceous slate follows the general law of thin-layered rock strength. Specifically, as β increases, the long-term strength decreases initially and then increases subsequently, and the long-term strength exhibits an ω-related strengthening effect and intermediate principal stress strengthening effect (Liu et al., 2023).

The failure mode and creep strain-time curves of siliceous slate under different loading angles and stress differences (σ_2-σ_3) are illustrated in Figs. 8 and 9. Figs. 8 and 9 indicate that there are significant differences in the failure modes and creep strain-time curves of siliceous slate under different loading angles and stress differences. Due to the intermediate principal stress level in the experiment being relatively low, it can be seen that, at any loading angle and stress difference, there is always compressive deformation in the σ_1 direction and expansive deformation in the σ_2 and σ_3 directions; under different loading angles and stress differences, the deformations in the σ_2 and σ_3 directions are different, which is related to the variation of the main fracture surface position. Three situations may be investigated separately: (a) When the stress difference is small (σ_2-σ_3 = 2/7/12/17 MPa) and $\omega = 0°$, the main fracture surface is parallel to the σ_2 direction, resulting in significant deformation in the σ_3 direction; (b) When the stress difference is small (σ_2-σ_3 = 7 MPa) and $\omega = 90°$, the main fracture surface is parallel to the σ_3 direction, resulting in significant deformation in the σ_2 direction; (c) When the stress difference is large (σ_2-σ_3 = 27/47 MPa), the main fracture surface is less affected by loading angle,

Table 2
True triaxial creep compression test scheme for siliceous slate.

Stress (MPa)		Loading angle (°)		Loading step (σ_1 (MPa)/time of duration (h))							
σ_3	σ_2	β	ω	step1	step2	step3	step4	step5	step6	step7	step8
3	5	90	/	139.5/12	153.4/0.2	/	/	/	/	/	/
	10	0	0	41.8/24	46.8/24	56.8/24	66.8/24	76.8/24	86.8/26	101.8/24	115.1/13.4
		0	90	68.5/9	99.6/12	119.6/12	135/0.3	/	/	/	/
		30	0	15/24	22.5/24	32.5/24	42.5/24	52.3/1.9	/	/	/
		30	90	62.2/10	93.4/12	109/0.2	/	/	/	/	/
		60	90	88.8/18	105.4/4.6	/	/	/	/	/	/
		75	0	62.3/24	93.3/10	114.5/14	125.1/10	132.5/11	143.3/0.1	/	/
		90	/	124.5/12	149.5/11	166.1/8	/	/	/	/	/
	15	75	0	114.6/12	127/0.3	/	/	/	/	/	/
	20	45	0	54.7/16	63.5/12	70.3/0.1	/	/	/	/	/
	30	30	90	45/11	55/12	65/12	80/12	95/12	104.8/4	/	/
	50	0	0	85/11	102/11	117/2.6	/	/	/	/	/
		30	90	57.1/11	74.4/13	86.8/10	104/12	114/11	122/12	128.4/9	133.4/2.8

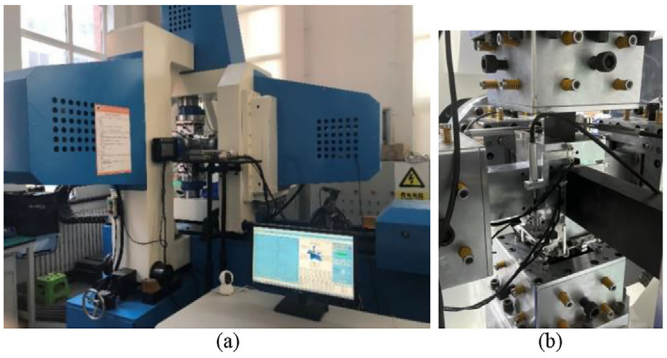


Fig. 4. (a) True triaxial testing apparatus, and (b) True triaxial rigid loading cell (modified after Feng et al., 2023).

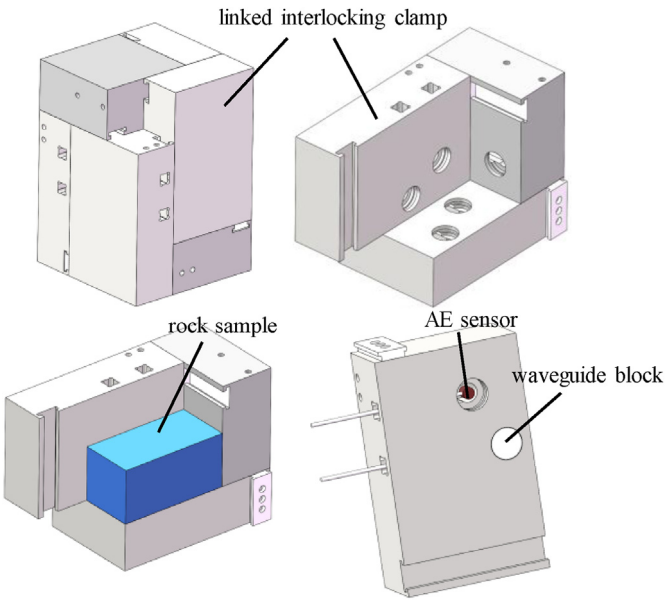


Fig. 5. Schematic diagram of linked interlocking clamp and placement of AE sensors (modified after Feng et al., 2023).

more specifically, the main fracture surface is parallel to the σ_2 direction.

Detailed investigation of the failure mode shows that: (a) when the stress difference is small (σ_2-σ_3 = 2/7/12/17 MPa), the failure

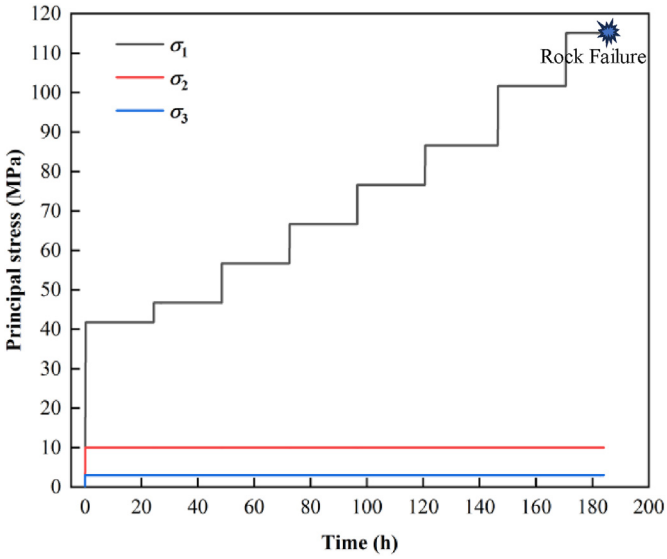


Fig. 6. Specific loading stages used in the true triaxial creep compression test at $\beta = \omega = 0°$.

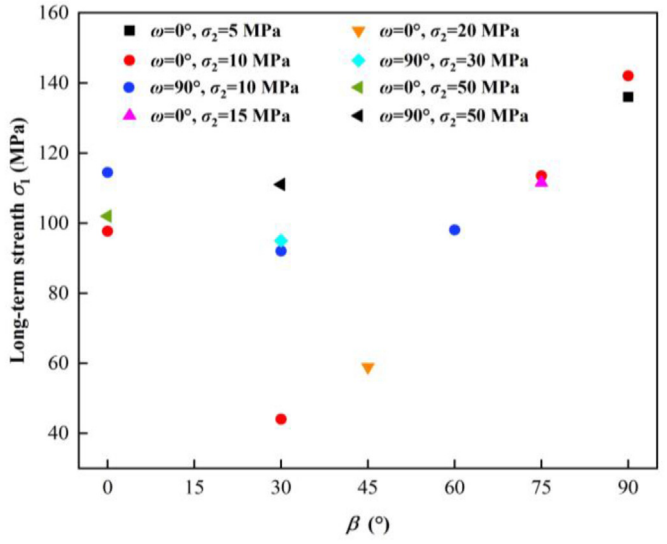


Fig. 7. Long-term strength of siliceous slate at different loading angles and σ_2 under true triaxial creep compression (σ_3 = 3 MPa).

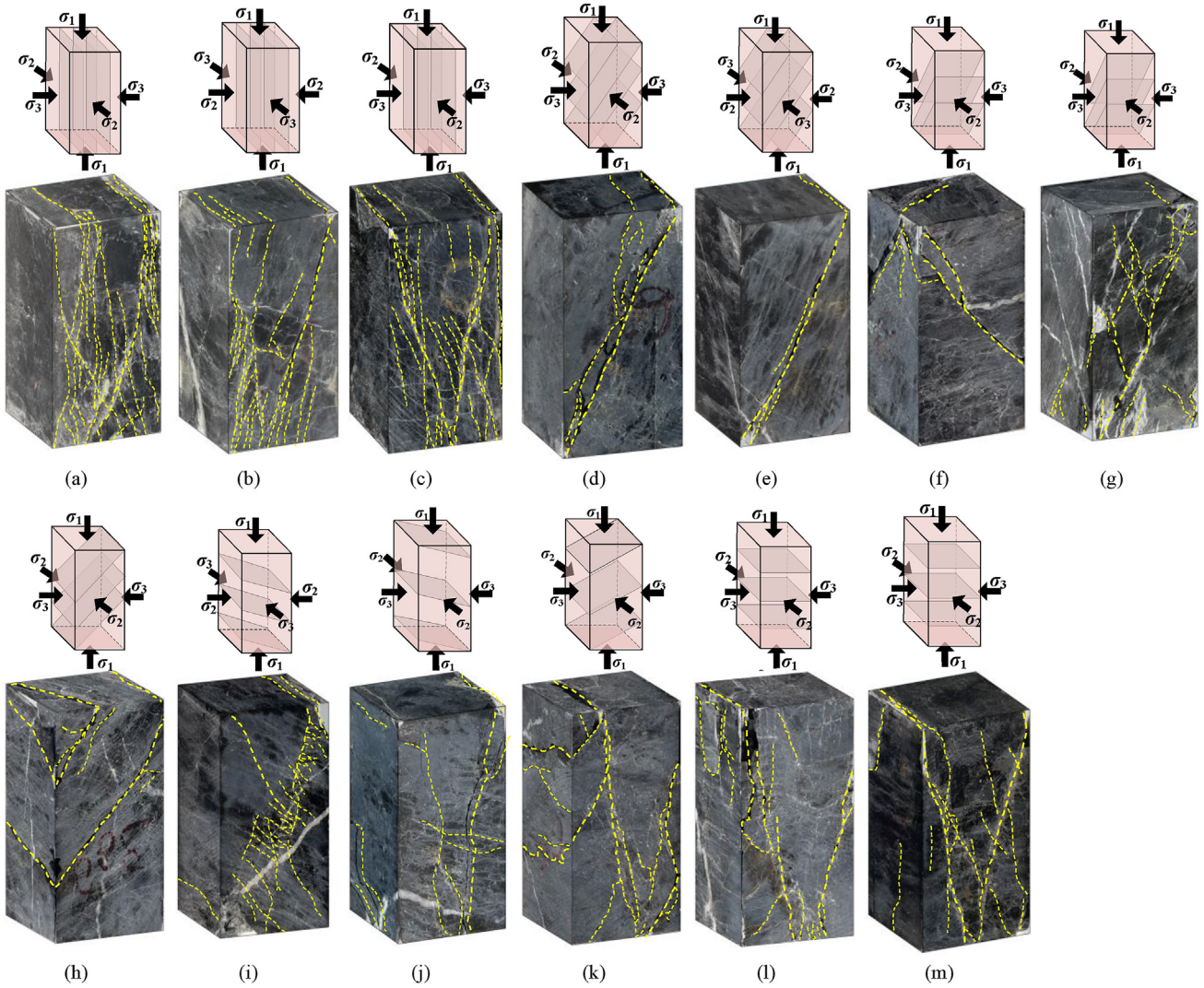


Fig. 8. Failure modes of siliceous slate at different loading angles and stress differences ($\sigma_3 = 3$ MPa): (a) $\beta = 0°$, $\omega = 0°$, $\sigma_2 = 10$ MPa, (b) $\beta = 0°$, $\omega = 90°$, $\sigma_2 = 10$ MPa, (c) $\beta = 0°$, $\omega = 0°$, $\sigma_2 = 50$ MPa, (d) $\beta = 30°$, $\omega = 0°$, $\sigma_2 = 10$ MPa, (e) $\beta = 30°$, $\omega = 90°$, $\sigma_2 = 10$ MPa, (f) $\beta = 30°$, $\omega = 90°$, $\sigma_2 = 30$ MPa, (g) $\beta = 30°$, $\omega = 90°$, $\sigma_2 = 50$ MPa, (h) $\beta = 45°$, $\omega = 0°$, $\sigma_2 = 20$ MPa, (i) $\beta = 60°$, $\omega = 90°$, $\sigma_2 = 10$ MPa, (j) $\beta = 75°$, $\omega = 0°$, $\sigma_2 = 10$ MPa, (k) $\beta = 75°$, $\omega = 0°$, $\sigma_2 = 15$ MPa, (l) $\beta = 90°$, $\sigma_2 = 5$ MPa, and (m) $\beta = 90°$, $\sigma_2 = 10$ MPa.

mode is the most complex at $\beta = 0°$, there are many macroscopic cracks during rock failure, multiple splitting cracks along bedding plane coexist with shear cracks passing through bedding plane (Fig. 8a–b), and the transition of the creep curve from the steady-state stage to the acceleration stage is slow (Fig. 9a–b), the creep curve exhibits progressive change feature. The failure mode is the simplest at $\beta = 30°/45°$, there is usually only one macroscopic shear slip crack along a bedding plane (Fig. 8d–e, h), the creep curve undergoes a sudden transition from the steady-state stage to the acceleration stage (Fig. 9d–e, h), and the creep curve exhibits sudden change feature. The failure mode of the sample is relatively complex at $\beta = 60°$, 75°, or 90°, some macroscopic cracks occur along the bedding plane and some passing through the bedding plane (Fig. 8i-m), the creep curve undergoes a relatively progressive transition from the steady-state stage to the acceleration stage (Fig. 9i-m), and the creep curve exhibits relatively progressive change; (b) When the stress difference is large (σ_2-$\sigma_3 = 47$ MPa) and $\omega = 0°$, the failure mode and shape of the creep curve are similar to those at a low stress difference (Figs. 8c and 9c). (c) When the stress difference is large (σ_2-$\sigma_3 = 27/47$ MPa) and $\omega = 90°$, the failure mode and shape of the creep curve are relatively less affected by bedding structure, and there are mainly mixed tensile-shear fractures that cross through bedding plane (Fig. 8f–g), the creep curve shows relatively progressive changes (Fig. 9f–g).

Possible explanations for the above phenomena can be summarized as follows: due to the presence of weak bedding planes, the failure mode of thin-layered rocks under true triaxial compression is jointly controlled by stress and bedding structure, that is, thin-layered rocks always tend to expand along the σ_3 direction and the normal to the bedding plane: (a) When $\omega = 0°$, the angle between the normal to the bedding plane and σ_3 direction is less than 90° and the angle between normal to the bedding plane and σ_2 direction is 90°, that is, the projection of the normal direction of the bedding plane in the σ_2 direction is 0, while the projection in the σ_3 direction is greater than 0. Under these conditions, the effects of stress and structure are synergistic, and the deformation in σ_3 direction is larger. (b) When $\omega = 90°$, the spatial relationship between the normal direction of the bedding plane and σ_2, σ_3 is contrary to that when $\omega = 0°$. Under these conditions, the stress effect is in competition with the structure effect, if the stress difference is small (σ_2-$\sigma_3 = 7$ MPa), the bedding structure plays a dominant role in the failure of the specimen, and the

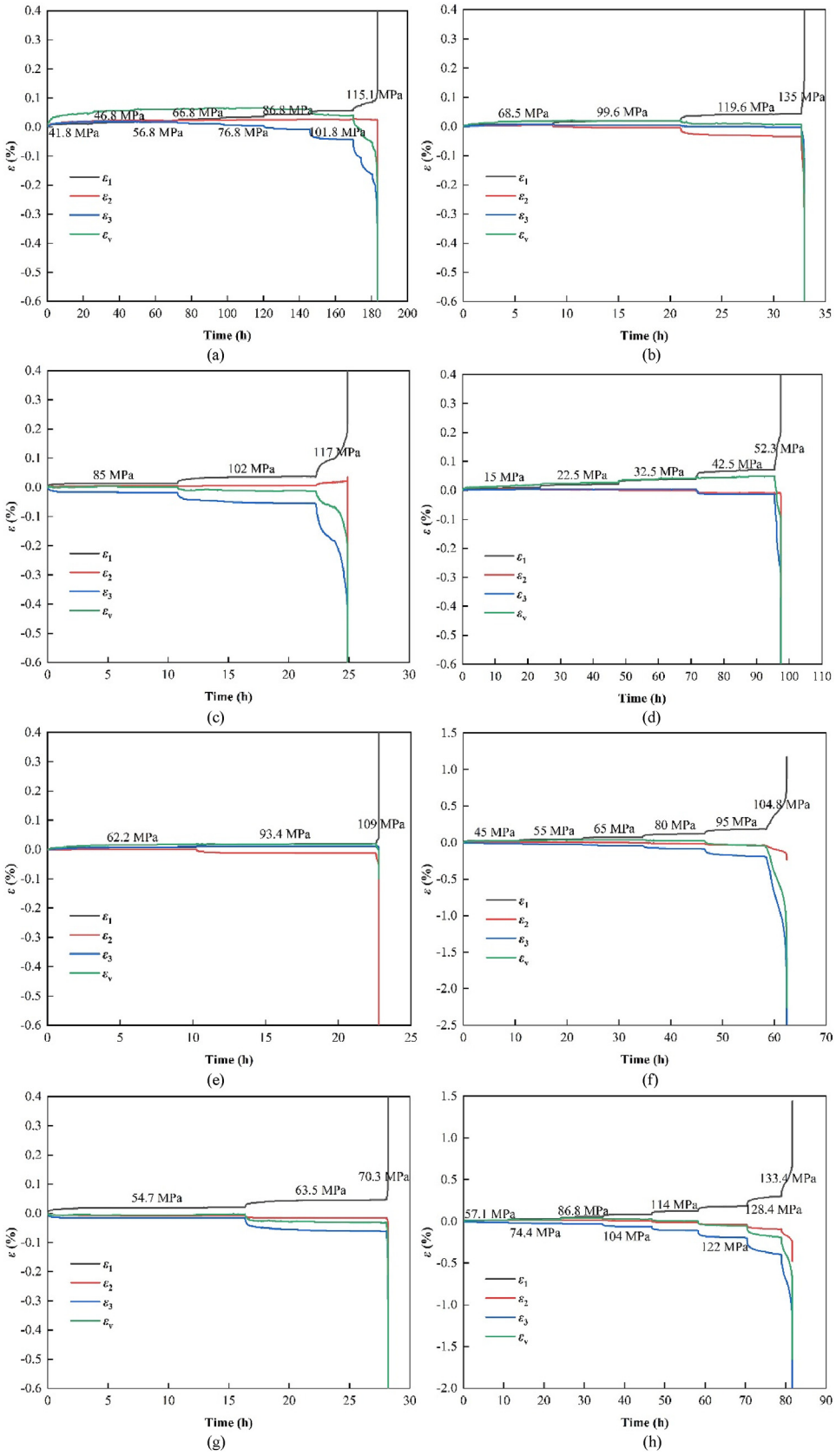


Fig. 9. Creep strain-time curves of siliceous slate at different loading angles and stress differences ($\sigma_3 = 3$ MPa): (a) $\beta = 0°$, $\omega = 0°$, $\sigma_2 = 10$ MPa, (b) $\beta = 0°$, $\omega = 90°$, $\sigma_2 = 10$ MPa, (c) $\beta = 0°$, $\omega = 0°$, $\sigma_2 = 50$ MPa, (d) $\beta = 30°$, $\omega = 0°$, $\sigma_2 = 10$ MPa, (e) $\beta = 30°$, $\omega = 90°$, $\sigma_2 = 10$ MPa, (f) $\beta = 30°$, $\omega = 90°$, $\sigma_2 = 30$ MPa, (g) $\beta = 30°$, $\omega = 90°$, $\sigma_2 = 50$ MPa, (h) $\beta = 45°$, $\omega = 0°$, $\sigma_2 = 20$ MPa, (i) $\beta = 60°$, $\omega = 90°$, $\sigma_2 = 10$ MPa, (j) $\beta = 75°$, $\omega = 0°$, $\sigma_2 = 10$ MPa, (k) $\beta = 75°$, $\omega = 0°$, $\sigma_2 = 15$ MPa, (l) $\beta = 90°$, $\sigma_2 = 5$ MPa, and (m) $\beta = 90°$, $\sigma_2 = 10$ MPa.

deformation in the σ_2 direction is relatively large, however, if the stress difference is large (σ_2-σ_3 = 27/47 MPa), the stress plays a dominant role in the failure of the specimen, and the deformation in the σ_3 direction is relatively large.

Different from instantaneous compression tests, under true triaxial creep compression, not only the fracture orientation but the fracturing process of thin-layered rocks can be jointly controlled by the stress and bedding structure. Under instantaneous compression, the deformation rate of specimen is usually controlled by the choice of experimental method. However, under true triaxial creep compression, the deformation and failure process of the specimen is divided into progressive failure and sudden failure. Two situations may be distinguished: (a) Under structure control, the sample mainly undergoes splitting tensile fracture or shear-slip failure along bedding plane. When $\beta = 0°$, during early stage of loading, the specimen undergoes splitting and tensile fracture along bedding plane, after a certain number of tensile cracks occur, the mechanical properties of the specimen deteriorate, resulting in macroscopic shear cracks passing through bedding plane. Ultimately, the failure of the specimen occurs. Therefore, the specimen has already produced many fractures along bedding plane before failure, and the creep curve of the sample exhibits progressive characteristic. When $\beta = 30°/45°$, the sample produces microcracks that slip along bedding plane during early loading stage. Due to the poor shear resistance of bedding plane, when the number of shear cracks is small, the sample undergoes macroscopic shear-slip along bedding plane, leading to macroscopic failure. Therefore, the sample does not undergo significant deformation before

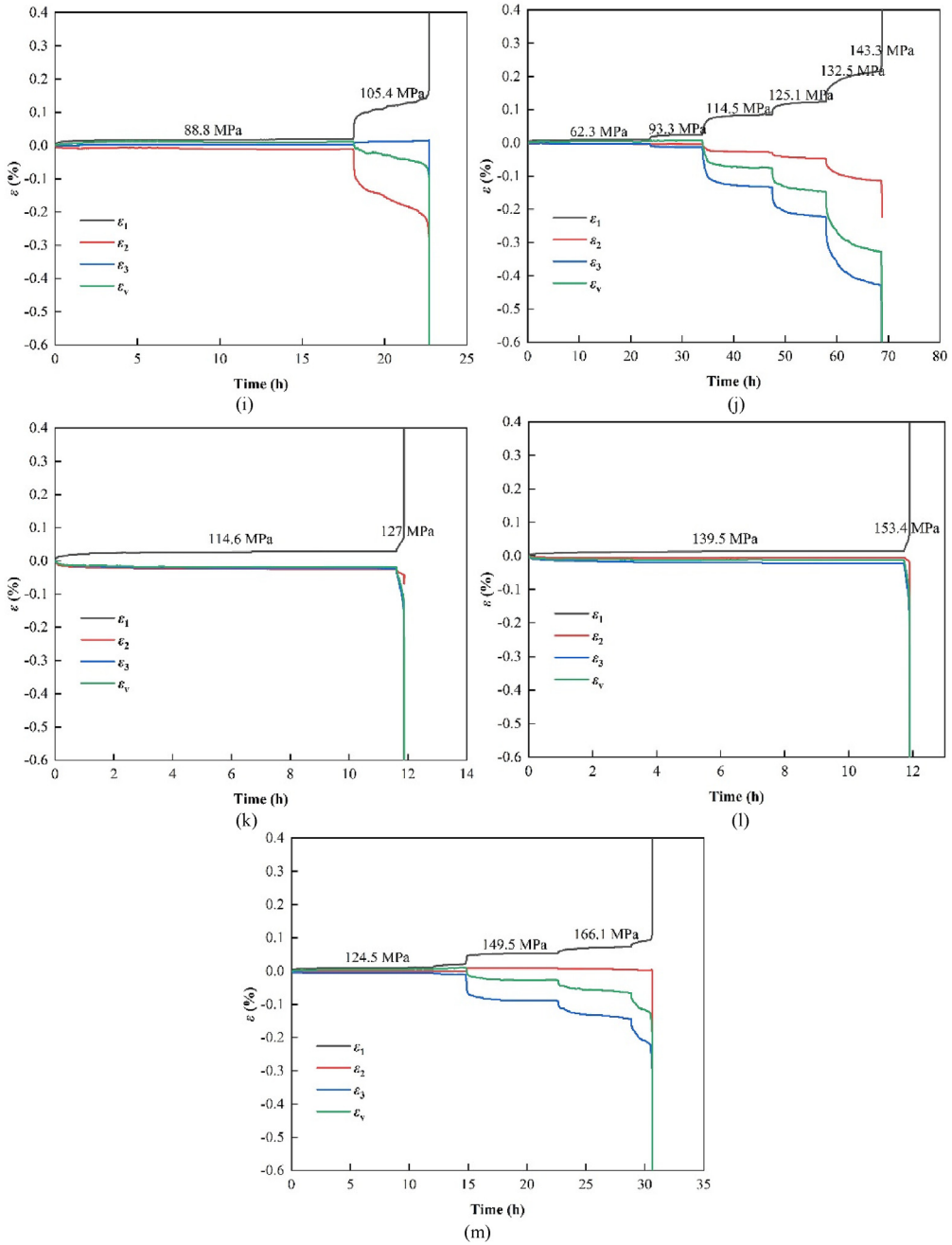


Fig. 9. (*continued*).

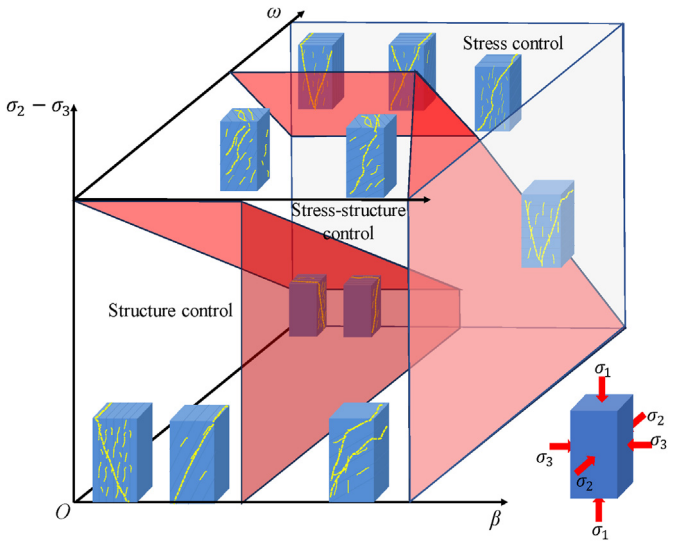


Fig. 10. 3D zoning map of the failure control mechanism of thin-layered rock at different loading angles and stress differences under true triaxial creep compression.

macroscopic failure, resulting in a sudden change in the creep curve; (b) Under stress control, the failure mode of the sample is mainly controlled by stress, the sample mainly generates mixed tensile-shear fractures through the bedding plane. In the early stage of loading, the specimen undergoes tensile fracturing with cracks passing through the bedding plane. When a certain number of micro-tensile cracks are generated, the mechanical properties of the specimen deteriorate, resulting in macroscopic shear cracks that pass through the bedding plane. Therefore, the creep curves are between progressive change to sudden change.

Based on the experimental results, it can be further inferred that, when loading angles β and ω are small (usually less than 45°), the effects of stress and structure are synergistic, but the tensile/shear fracture mode of rocks varies under different loading angles. Therefore, it is defined that rock failure is controlled by structure in this case. When β is small (usually less than 45°–60°) and ω is large (usually larger than 45°), the stress effect is in competition with the structure effect. If the stress difference is small, the bedding structure plays a dominant role in the failure of the specimen, it is defined that rock failure is controlled by structure in this case, otherwise, rock failure is controlled by stress. When β is large (usually larger than 75°), the failure of rocks is minimally affected by the structure, rock failure is controlled by stress. The failure mechanisms of thin-layered rock at different loading angles and stress differences are shown in Fig. 10.

3.2. AE characteristics of siliceous slate

The AE characteristics of siliceous slate under true triaxial creep compression were analyzed, and its fracture evolution process assessed based on the AE localization method. The evolutions of AE

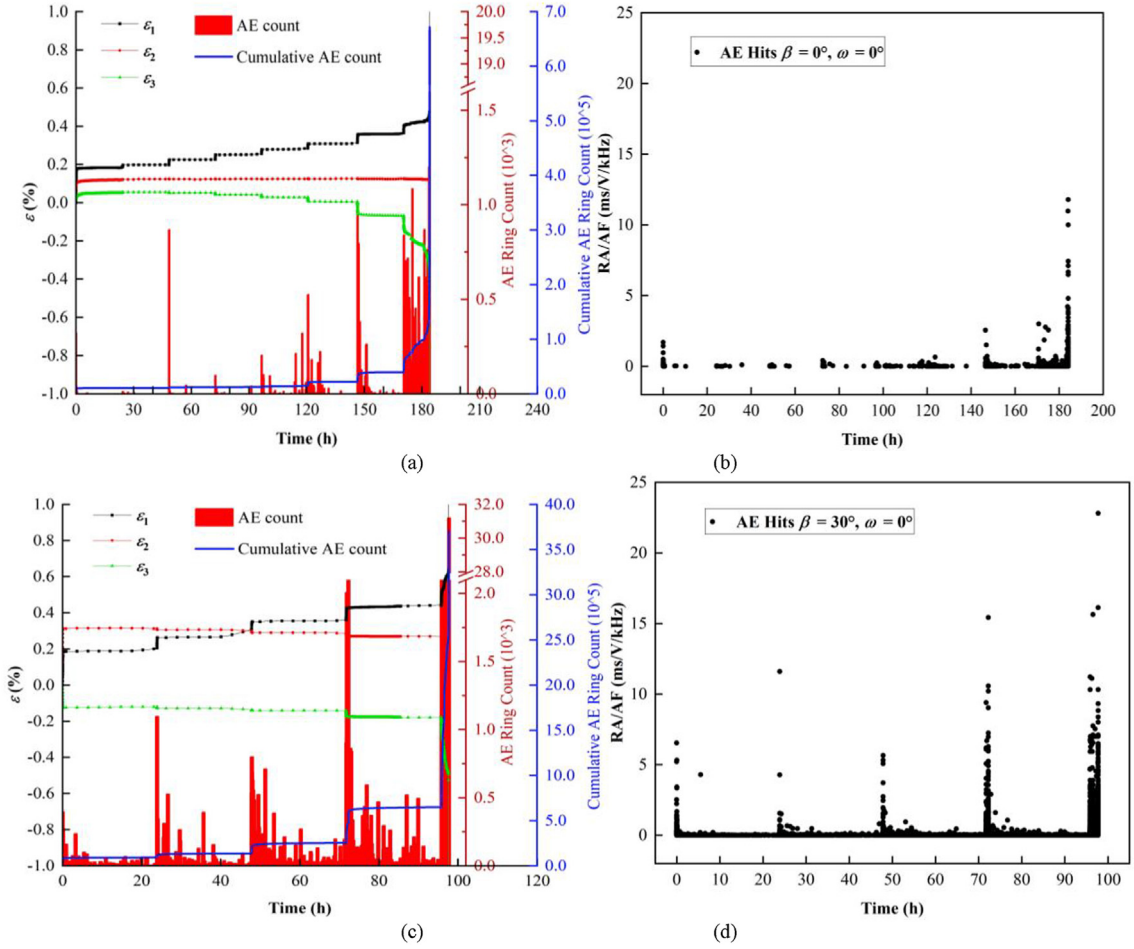


Fig. 11. AE characteristics of siliceous slate at different loading angles and $\sigma_2 = 10$ MPa, $\sigma_3 = 3$ MPa: (a) Ring count at $\beta = 0°$, $\omega = 0°$, (b) RA/AF at $\beta = 0°$, $\omega = 0°$, (c) Ring count at $\beta = 30°$, $\omega = 0°$, and (d) RA/AF at $\beta = 30°$, $\omega = 0°$.

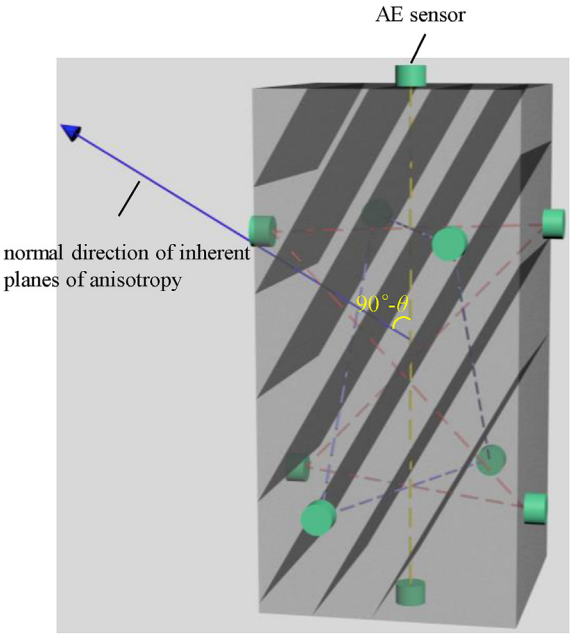


Fig. 12. Schematic diagram of rock sample wave velocity measurement (modified after Song et al., 2024).

ring counts and rise time/amplitude (RA) to average frequency (AF) values of siliceous slate under different loading angles over time are shown in Fig. 11. RA/AF was used to determine the crack type (Ohno and Ohtsu, 2010), when AF is high and RA is low, the crack can be regarded as a tensile crack; when AF is low and RA is high, it can be regarded as a shear crack. Fig. 11 shows that under different loading angles, the cumulative AE ring counts of siliceous slate increase in a step-wise manner during step-loading in the creep process, and the AE ring counts of the last loading level are far greater than those in the previous stages, indicating that the fracturing of the sample has developed throughout the entire creep-loading process, but the majority of fractures occur during the last creep loading stage. The RA/AF values of the samples are relatively small in the early stage of loading and when the sample approaches failure, the RA/AF values are relatively large, indicating that tensile fractures were generated therein, with shear fractures being developed later.

Due to the high anisotropy of thin-layered rock, the wave velocity of thin-layered rock is greatly influenced by bedding structure. In addition, due to the discreteness between samples, it is inappropriate to use a unified formula to describe the properties of all samples. It is therefore suggested to measure the P-wave velocities of each sample in different directions, establish empirical formulas relating P-wave velocities and angle θ (the angle between the direction of wave propagation and the bedding plane, $0^\circ \le \theta \le 90^\circ$) in each sample (Song et al., 2024). AE acquisition apparatus has the function of transmitting pulse waves through AE sensors. Each sensor can emit pulse waves which are received by all other sensors, from which the travel times of the waves between any two sensors can be determined. According to travel times and sensor coordinates, the wave velocities of rock samples in different directions can be calculated. To avoid pulse wave transmission to the sensors through the linked interlocking clamp rather than the rock sample and ensure that the measured velocities are the wave velocities of rock samples, only those data from each pair of sensors on opposite planes are used. Fig. 12 shows the measurement method of wave velocity, the two sensors connected by the dashed line are used to measure the wave velocity in the corresponding direction. Therefore, a set of data of anisotropic P-wave velocities and angle θ can be obtained, then the functional relationship between angle θ and P-wave velocities is expounded by fitting this set of data. The measured wave velocity of the samples used in this article and anisotropic wave velocity models used for AE localization are summarized in Table 3. In Table 3, $\theta_0 = 1^\circ$ and $v_0 = 1$ m/s, θ_0 and v_0 are used to ensure that the units on both sides of the equations are equivalent. To investigate the fracture behavior of siliceous slate during different stages of creep loading, the creep loading process is divided into five stages (1–5) for AE localization. Before the last level of creep loading demarcates the first stage (1), and the last level of creep loading is equally divided into four stages (2–5): the localization results are shown in Fig. 13.

As shown in Figs. 11 and 13, when $\beta = 0^\circ$ and $\omega = 0^\circ$, the RA/AF values of the sample are small during the loading process, and only increase when the sample approaches failure. The locations of the fractures are relatively scattered in the early loading stage, and only in the final stage did the fractures occur at a concentrated location. When $\beta = 30^\circ$ and $\omega = 0^\circ$, the RA/AF values of the specimen are relatively high throughout the loading process. The locations of the fractures are concentrated throughout the entire loading process and develop along the bedding plane. This indicated that, when $\beta = 0^\circ$ and $\omega = 0^\circ$, multiple tensile splitting fractures occur along the bedding plane in the early stage of loading, resulting in the deterioration of mechanical properties of the specimen, and macroscopic shear cracks passing through bedding plane later. When $\beta = 30^\circ$ and $\omega = 0^\circ$, due to the weak adhesion between bedding planes, shear fractures occur along bedding plane throughout the entire loading process. As the load increases, the shear resistance between bedding planes is insufficient to support the shear force, leading to macroscopic shear sliding failure of the sample along the bedding plane.

4. A 3D anisotropic visco-plastic creep model for thin-layered rock

4.1. Formulation and parametric analysis of the model

4.1.1. Basic requirements and specific form of the model

According to the long-term strength, deformation and fracture characteristics revealed by the true triaxial creep compression test of thin-layered rocks, the 3D anisotropic creep model should meet the following requirements: (i) The model should be able to reflect the anisotropic long-term strength, failure process and fracture orientation of thin-layered rocks under the coupling effect of inherent anisotropy and intermediate principal stress; and (ii) The model should be able to reflect the three creep stages, namely the

Table 3
Anisotropic P-wave velocities and models for siliceous slate samples ($\sigma_2 = 10$ MPa, $\sigma_3 = 3$ MPa).

Loading angle	Anisotropic wave velocities						P-wave velocity model (m/s)
$\beta = 0^\circ$, $\omega = 0^\circ$	θ (°)	0	18.5	56.4	71.5		$v = \left[0.2586\left(\frac{\theta}{\theta_0}\right)^2 - 39.79\frac{\theta}{\theta_0} + 2858\right]v_0$
	Wave velocity (m/s)	2849.3	2226.5	1417	1345.5		
$\beta = 30^\circ$, $\omega = 0^\circ$	θ (°)	16.1	26.4	30	55.2	86.4	$v = \left[0.2433\left(\frac{\theta}{\theta_0}\right)^2 - 36.29\frac{\theta}{\theta_0} + 2116\right]v_0$
	Wave velocity (m/s)	1667.4	1327.5	1111.5	941.8	775.8	

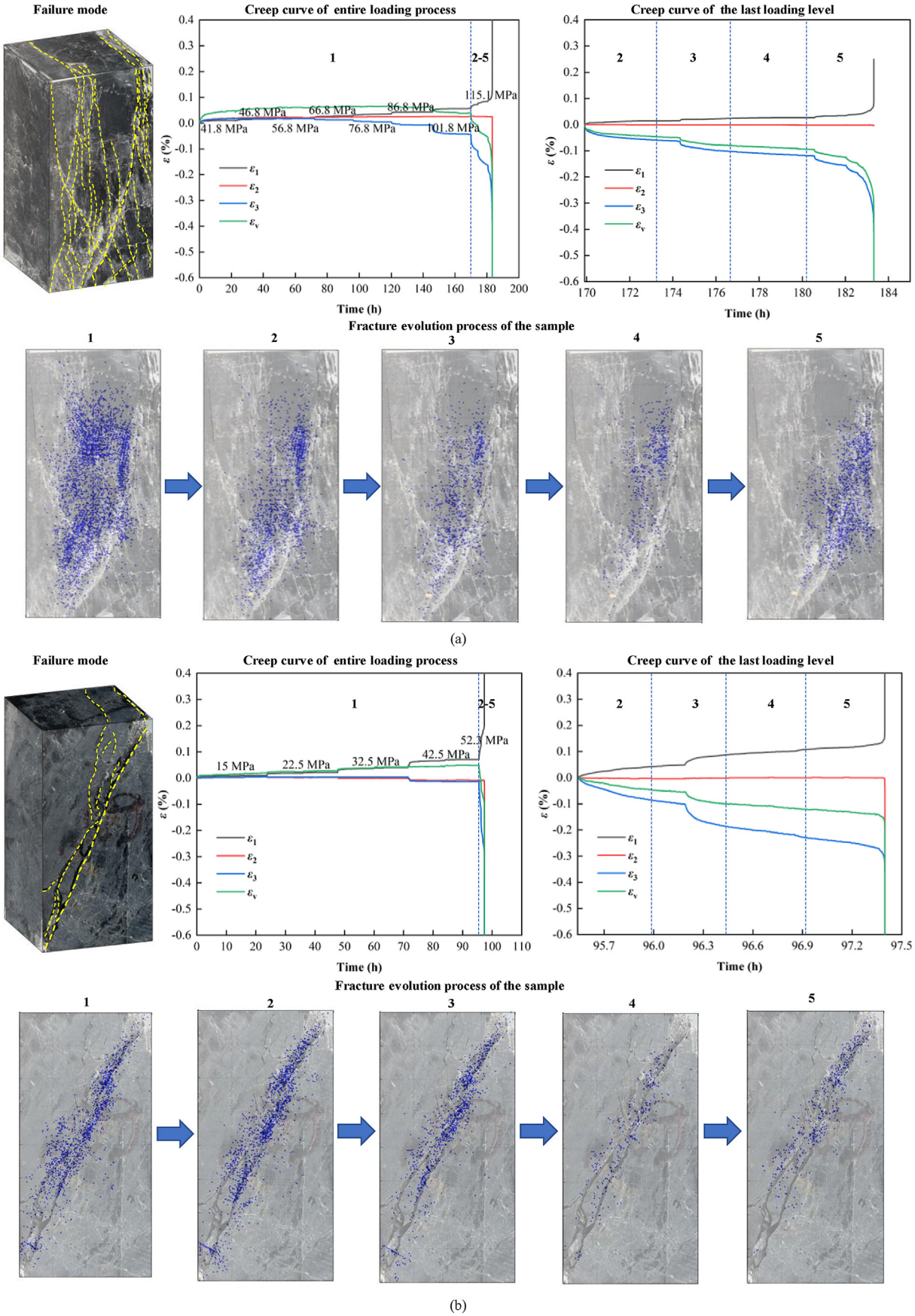


Fig. 13. Fracture evolution process of specimen under different loading angles and $\sigma_2 = 10$ MPa, $\sigma_3 = 3$ MPa (1–5 represents the five different stages of each creep-loading test): (a) $\beta = 0°$, $\omega = 0°$, and (b) $\beta = 30°$, $\omega = 0°$.

decelerating creep, steady-state creep, and accelerating creep stages.

In visco-plastic theory and Perzyna's overstress theory, the total strain rate tensor $\dot{\varepsilon}_{ij}$ can be decomposed into elastic and visco-plastic components, as shown in Eqs. (1)–(3). Since this paper mainly explores the creep failure characteristics of thin-layered rocks, therefore, the visco-plastic deformation corresponding to the fracture process of thin-layered rocks is mainly discussed in this section.

$$\dot{\varepsilon}_{ij} = \dot{\varepsilon}_{ij}^{\mathrm{e}} + \dot{\varepsilon}_{ij}^{\mathrm{vp}} \tag{1}$$

$$\dot{\varepsilon}_{ij}^{\mathrm{e}} = D_{ij}\dot{\sigma}_{ij} \tag{2}$$

$$\dot{\varepsilon}_{ij}^{\mathrm{vp}} = \lambda\langle\Phi(F)\rangle\frac{\partial Q}{\partial\sigma_{ij}} \tag{3}$$

where $\dot{\varepsilon}_{ij}^{\mathrm{e}}$ represents the elastic strain rate tensor, $\dot{\varepsilon}_{ij}^{\mathrm{vp}}$ is the visco-plastic strain rate tensor, D_{ij} is the elastic compliance matrix, $\dot{\sigma}_{ij}$ denotes the stress rate tensor, λ is a viscosity parameter (unit: s^{-1}) used to define the magnitude of the visco-plastic strain rate. $\langle\Phi(F)\rangle$ is a function of the overstress F, representing the distance between the current stress state and the envelope surface of 3D time-dependent failure criterion; $<\ >$ is the Macaulay bracket, when $\Phi(F)>0$, $\langle\Phi(F)\rangle = \langle\Phi(F)\rangle$, when $\Phi(F)<0$, $\langle\Phi(F)\rangle = 0$; Q denotes the plastic potential function that determines the direction of the visco-plastic strain rate based on the visco-plastic flow rule. The specific form of the model is shown in Eqs. (4)–(6);

$$\dot{\varepsilon}_{ij}^{\mathrm{vp}} = \lambda\left[\frac{F(\bar{\varepsilon}^{\mathrm{p}})}{F_0}\right]^N\frac{\partial Q}{\partial\sigma_{ij}} \tag{4}$$

$$\lambda = \lambda_1 + \lambda_2 e^{-a\frac{\bar{\varepsilon}_0^{\mathrm{p}}}{\bar{\varepsilon}_{\mathrm{e}}^{\mathrm{p}}}} \tag{5}$$

$$\bar{\varepsilon}^{\mathrm{p}} = \frac{2}{90}\sqrt{(\varepsilon_1-\varepsilon_2)^2+(\varepsilon_1-\varepsilon_3)^2+(\varepsilon_2-\varepsilon_3)^2} \tag{6}$$

where F_0 is the long-term strength of specimen under true triaxial creep compression, N is the overstress index, λ_1 and λ_2 are the visco-plastic flow coefficients, ε_1, ε_2 and ε_3 are the principal strains corresponding to three principal stresses, respectively, $\bar{\varepsilon}^{\mathrm{p}}$ is the equivalent strain, $\bar{\varepsilon}_0^{\mathrm{p}}$ is the equivalent strain at initial loading, $\bar{\varepsilon}_{\mathrm{e}}^{\mathrm{p}}$ is the equivalent strain at the end of loading, and a is the attenuation coefficient of the visco-plastic flow coefficient, characterizing the rate of decrease in the visco-plastic flow coefficient.

4.1.2. 3D time-dependent failure criterion

To obtain the overstress equation F, the first step is to establish a 3D time-dependent failure criterion of thin-layered rocks. Feng et al. (2020) and Liu et al. (2023) proposed a true triaxial failure criterion for anisotropic rock based on Mohr-Coulomb failure criterion. The criterion considered the friction angle φ as a function related to stress state parameter b and the cohesion c as a function related to the loading angles and b to reflect the variation in strength with loading angles and stress state:

$$\sigma_1 = \frac{1+\sin\varphi_b}{1-\sin\varphi_b}\sigma_3 + \frac{2c_{\beta\omega b}\cot\varphi_0\sin\varphi_b}{1-\sin\varphi_b} \tag{7}$$

$$c_{\beta\omega b} = \frac{c_{90}}{1+A[\cos 2\beta_{\min}+\cos 2(\beta-\beta_{\min})]^n}\left\{1+D\left[\sin\omega\cos\frac{\pi(\beta-\beta_{\max})}{\pi-2\beta_{\max}}\right]^{\frac{1}{m}}b^m\right\} \tag{8}$$

$$\sin\varphi_b = \frac{\sin\varphi_0}{\sqrt{1-b+sb^2}+t\left(1-\sqrt{1-b+b^2}\right)\sin\varphi_0} \tag{9}$$

$$b = \frac{\sigma_2-\sigma_3}{\sigma_1-\sigma_3} \tag{10}$$

where φ_b is the friction angle with respect to different b values; φ_0 is the friction angle at $b = 0$, $c_{\beta\omega b}$ is the cohesion with respect to different β, ω and b values; c_{90} is the cohesion at $\beta = 90°$; $\beta_{\min}$ is the angle at which the strength is at the lowest point of the 'U' shape curve under conventional triaxial compression; $\beta_{\max}$ is the angle at which the strength is most affected by ω; s, t, A, n, D, and m are material constants, s and t describe the effect of σ_2 on the strength; A and n affect the degree of anisotropy of strength and the shape of U-shaped curve under conventional triaxial compression; D and m affect the degree of influences of ω and b on the strength under true triaxial compression. This article mainly studies the failure characteristics of thin-layered rocks under true triaxial creep compression, the direct tensile failure characteristics of thin-layered rocks are not within the scope of this study. In order to reflect the failure characteristics of rocks in the tensile stress zone, the failure criterion (Eq. (7)) can be used as the asymptotic line of failure strength, and a hyperbolic function can be used to modify the failure criterion nonlinearly. Detailed failure criterion modification and parameter identification methods can be found in Feng et al. (2020) and Liu et al. (2023).

Based on the true triaxial failure criterion for anisotropic rock, it is believed that rock fracture leads to the loss of cohesion, and the time-dependent fracture damage of rocks is reflected through the weakening of cohesion over time. The 3D time-dependent failure criterion is expressed as follows:

$$F(\bar{\varepsilon}^{\mathrm{p}}) = \sigma_1(1-\sin\varphi_b)-\sigma_3(1+\sin\varphi_b)-2Ic_{\beta\omega b}\cot\varphi_0\sin\varphi_b \tag{11}$$

$$I = 1-\frac{\bar{\varepsilon}_x^{\mathrm{p}}}{\bar{\varepsilon}_{\mathrm{e}}^{\mathrm{p}}}, x = 0,1,2,3\ldots \tag{12}$$

where I is the time-dependent fracture coefficient, $0 \le I \le 1$. When $I = 1$, it indicates that the rock sample is in an undamaged initial state, and when $I = 0$, it indicates that the sample is in a completely fractured state; $\bar{\varepsilon}_x^{\mathrm{p}}$ is the equivalent strain during the true triaxial creep loading process, which can be calculated by the improved Euler iteration method:

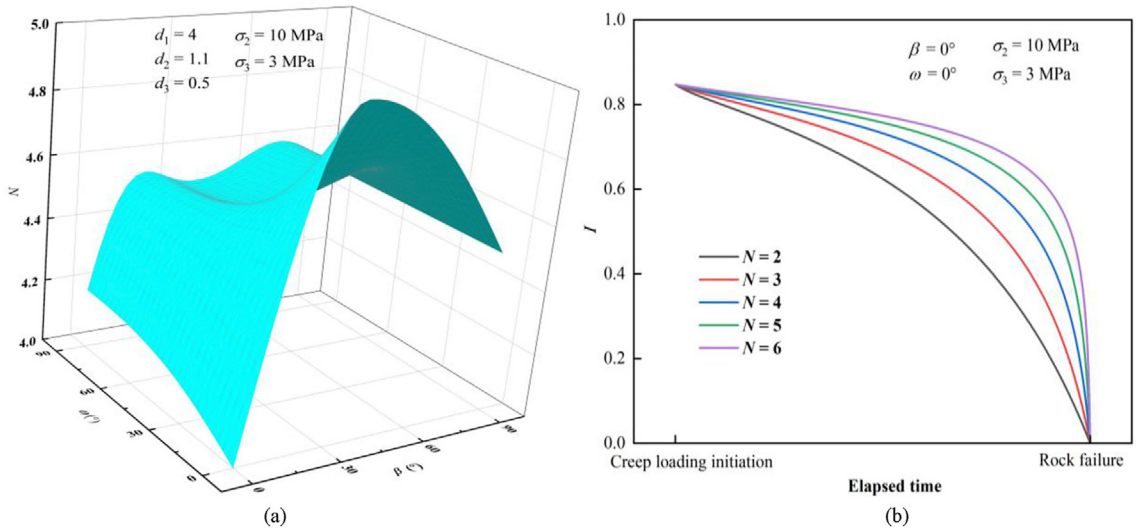


Fig. 14. (a) Variations of N under different β and ω values at $d_1 = 4$, $d_2 = 1.1$, $d_3 = 0.5$, $\sigma_2 = 10$ MPa and $\sigma_3 = 3$ MPa, and (b) Variations of I with time under different N values at $\beta = \omega = 0°$, $\sigma_2 = 10$ MPa and $\sigma_3 = 3$ MPa.

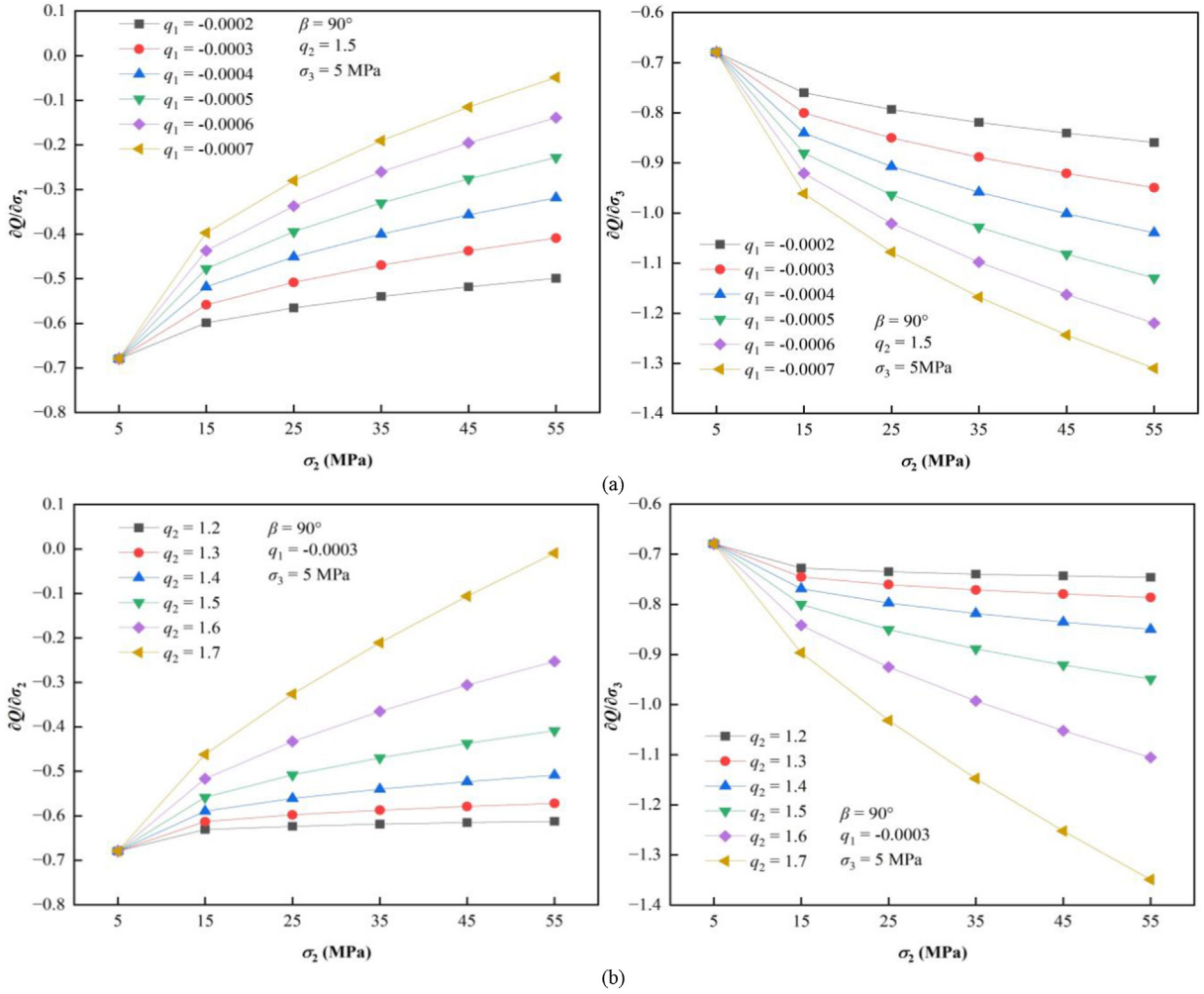


Fig. 15. Variations of $\frac{\partial Q}{\partial \sigma_2}$ and $\frac{\partial Q}{\partial \sigma_3}$ with σ_2 under true triaxial compression and $\beta = 90°$: (a) when taking different values of q_1, and (b) when taking different values of q_2.

$$\bar{\varepsilon}_{x+1}^{p}=\bar{\varepsilon}_{x}^{p}+\frac{\Delta t}{2}(K_1+K_2) \tag{13}$$

$$K_1=\lambda\left[\frac{F(\bar{\varepsilon}_{x}^{p})}{F_0}\right]^{N}\frac{\partial Q}{\partial \sigma_{ij}} \tag{14}$$

$$K_2=\lambda\left[\frac{F(\bar{\varepsilon}_{x}^{p}+\Delta t K_1)}{F_0}\right]^{N}\frac{\partial Q}{\partial \sigma_{ij}} \tag{15}$$

where Δt is the iteration time step.

4.1.3. Overstress index

The overstress index N mainly affects the shape of the creep curve from the steady creep stage to the accelerated creep stage. Therefore, the overstress index was constructed related to loading angles (β, ω) and stress state parameter b to reflect the anisotropic creep fracturing process of rocks at different loading angles and stress states. The specific form of N is shown in Eq. (16):

$$N=\begin{cases}\dfrac{d_1+\sin\dfrac{\pi\beta}{2\beta_{\min}}}{1+d_2\sin\omega\sin\dfrac{\pi(3\beta-\beta_{\min})}{4\beta_{\min}}b}(0<\beta<\beta_{\min})\\[2ex]\dfrac{d_1+d_3\cos\dfrac{\pi(\beta-\beta_{\min})}{\pi-2\beta_{\min}}+1-d_3}{1+d_2\sin\omega\cos\dfrac{\pi(\beta-\beta_{\min})}{\pi-2\beta_{\min}}b}(\beta\geq\beta_{\min})\end{cases} \tag{16}$$

where d_1, d_2, and d_3 are overstress index parameters, d_1 mainly affects N at $\beta=\omega=0°$, d_2 mainly affects the degree of influences of ω and b on N, d_3 mainly affects N at $\beta=90°$. Taking siliceous slate used in this paper as an example, the variations of N under different β and ω values at $d_1=4$, $d_2=1.1$, $d_3=0.5$, $\sigma_2=10$ MPa and $\sigma_3=3$ MPa are shown in Fig. 14a. The variations of I with time under different N values at $\beta=\omega=0°$, $\sigma_2=10$ MPa and $\sigma_3=3$ MPa are presented in Fig. 14b. It can be seen that when N is large, I is quasi-constant in the early stage of loading, only when the rock approaches failure will I suddenly decrease. When N is small, the decrease rate of I is relatively uniform throughout the entire loading stage. Therefore, different N values can reflect the anisotropic failure process of thin-layered rocks under different loading angles and stress differences. N can be determined by creep

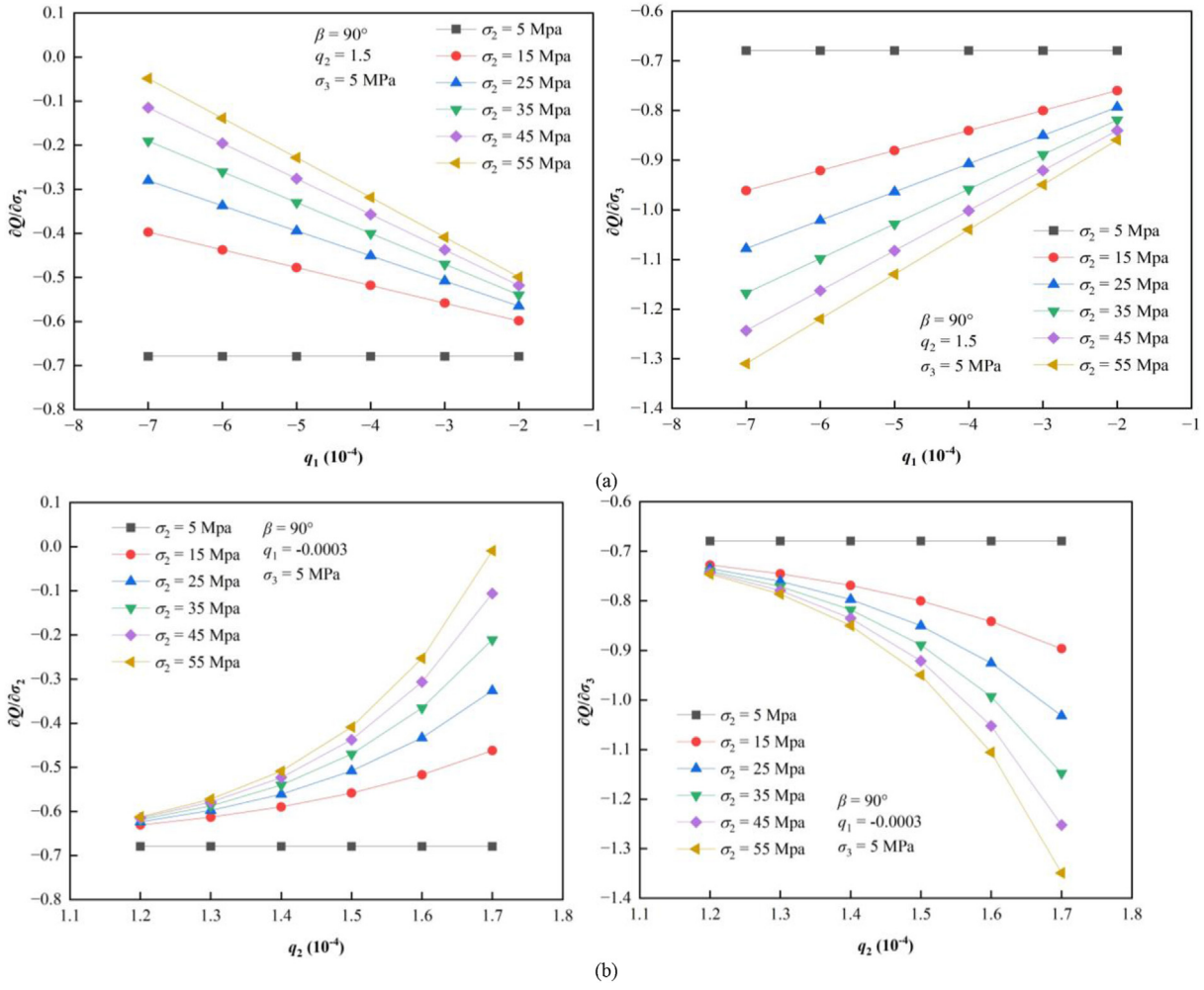


Fig. 16. Variations of $\frac{\partial Q}{\partial \sigma_2}$ and $\frac{\partial Q}{\partial \sigma_3}$ when taking different values of σ_2 under true triaxial compression and $\beta=90°$: (a) with the change in q_1, and (b) with the change in q_2.

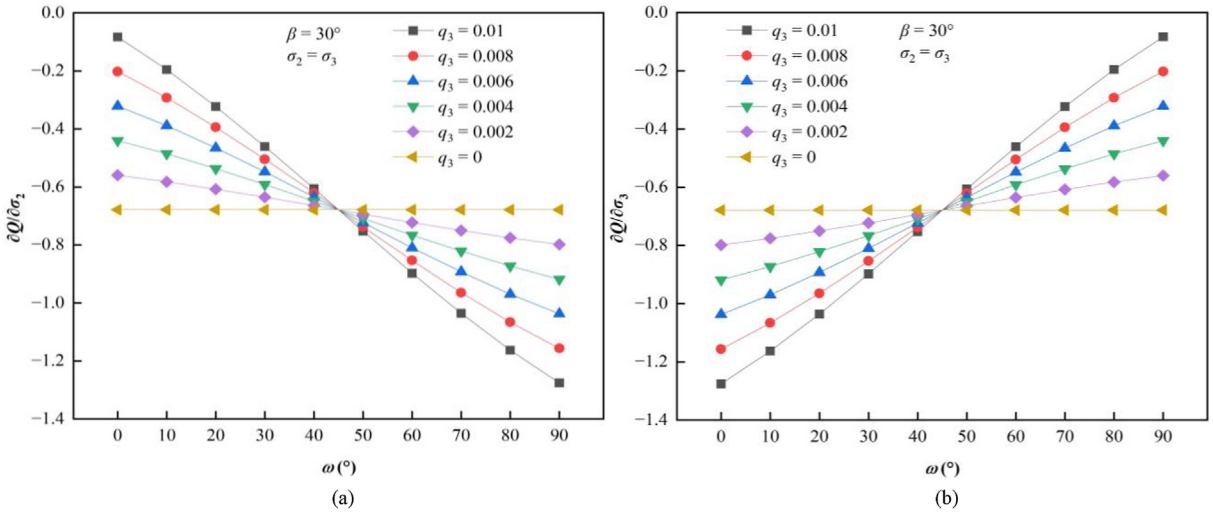


Fig. 17. Variations of (a) $\frac{\partial Q}{\partial \sigma_2}$ and (b) $\frac{\partial Q}{\partial \sigma_3}$ with ω when taking different values of q_3 under conventional triaxial compression.

Table 4
Long-term strength parameter identification results of siliceous slate.

Rock type	Parameters									
	s	t	c_{90} (MPa)	φ_0 (°)	β_{min} (°)	β_{max} (°)	A	n	D	m
Siliceous slate	0.98	0.88	45.5	21	33	25	1	2.7	2.0	0.45

deformation data of samples under different β, ω, and b values.

4.1.4. Plastic potential function

To reflect the variations in the fracture orientation of specimens with loading angles (β, ω) and stress state, non-associated flow rule was adopted, i.e., the plastic potential function is different from the time-dependent failure criterion. The specific form of the plastic potential function is shown in Eqs. (17) and (18):

$$Q = \sigma_1(1-\sin\varphi_0) - \sigma_3(1+\sin\varphi_0) - 2c_{90}\cos\varphi_0\left[q_1 p^{q_2} + \frac{1+\sin\varphi_0}{4\cos\varphi_0 c_{90}} p + \sin\left(\omega-\frac{\pi}{4}\right)\cos\frac{\pi(\beta-\beta_{max})}{\pi-2\beta_{max}}\cdot q_3 p\right] \quad (17)$$

$$p = \sigma_2 - \sigma_3 \quad (18)$$

where q_1, q_2, and q_3 are plastic potential function parameters, q_1 and q_2 represent the effect of the stress difference on the deformation of thin-layered rocks and q_3 represents the effect of bedding structure on deformation of thin-layered rocks. Within the scope of this paper, the partial derivative of the plastic potential function to the maximum principal stress is a constant (Eq. (19)), so this section mainly discusses the effect of plastic potential function parameters on $\frac{\partial Q}{\partial \sigma_2}$ and $\frac{\partial Q}{\partial \sigma_3}$. The partial derivatives of the plastic potential function with respect to the three principal stresses are shown in Eqs. (19)–(21):

$$\frac{\partial Q}{\partial \sigma_1} = 1 - \sin\varphi_0 \quad (19)$$

Table 5
Creep deformation parameter identification results of siliceous slate.

Loading angle	Stress difference (MPa)	Parameters								
		λ_1 (s^{-1})	λ_2 (s^{-1})	a	d_1	d_2	d_3	q_1	q_2	q_3
$\beta = 90°$	2	5.97×10^{-3}	1.8×10^{2}	−50	6	1.1	0.5	-2×10^{-4}	1.9	0.0084
$\beta = 0°, \omega = 0°$	7	1.33×10^{-5}	4							
$\beta = 0°, \omega = 90°$		4.18×10^{-3}	6×10^{3}							
$\beta = 30°, \omega = 0°$		4.99×10^{-3}	2×10^{3}							
$\beta = 30°, \omega = 90°$		2.31×10^{-5}	2×10^{2}							
$\beta = 60°, \omega = 90°$		9.26×10^{-5}	8×10^{3}							
$\beta = 75°, \omega = 0°$		2.64×10^{-2}	8×10^{3}							
$\beta = 90°$		2.05×10^{-5}	1.8×10^{2}							
$\beta = 75°, \omega = 0°$	12	3.22×10^{-3}	8×10^{3}							
$\beta = 45°, \omega = 0°$	17	2.22×10^{-3}	8×10^{3}							
$\beta = 30°, \omega = 90°$	27	2.15×10^{-3}	1×10^{2}							
$\beta = 0°, \omega = 0°$	47	1.85×10^{-4}	5×10^{3}							
$\beta = 30°, \omega = 90°$		6.18×10^{-5}	1×10^{3}							

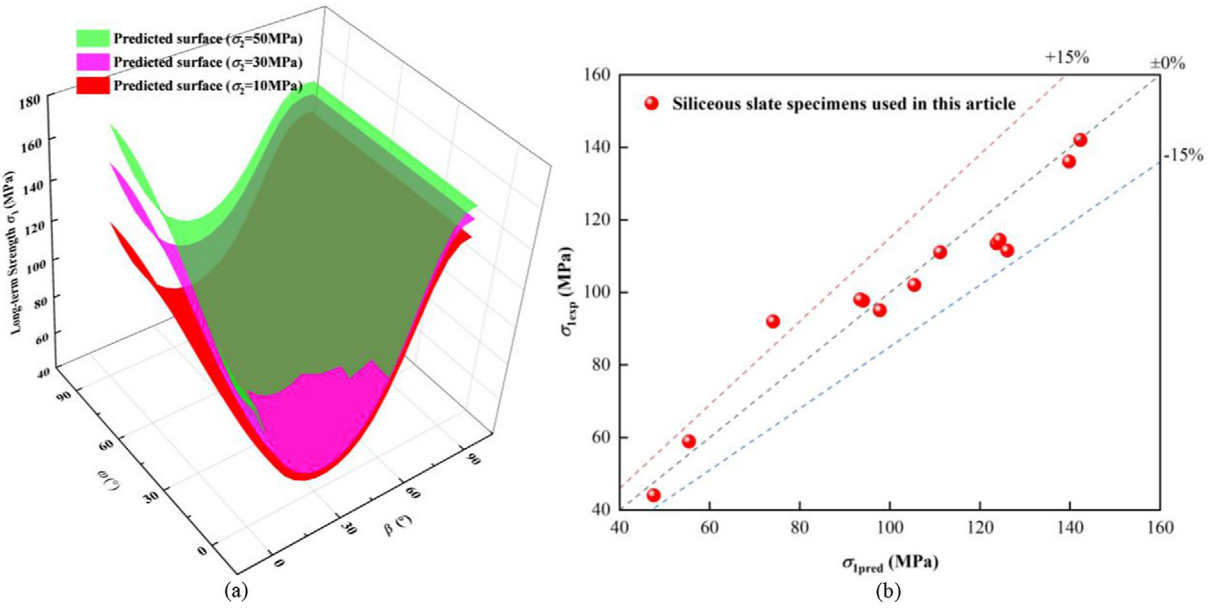


Fig. 18. (a) Predicted surfaces of long-term strength of siliceous slate under true triaxial creep compression, and (b) Comparison between experimental and predicted long-term strength results (σ_3 = 3 MPa).

$$\frac{\partial Q}{\partial \sigma_2} = -2c_{90}\cos\varphi_0\left[q_1q_2(\sigma_2-\sigma_3)^{q_2-1} + \frac{1+\sin\varphi_0}{4\cos\varphi_0 c_{90}} + \sin\left(\omega-\frac{\pi}{4}\right)\cos\frac{\pi(\beta-\beta_{\max})}{\pi-2\beta_{\max}}\cdot q_3\right] \tag{20}$$

$$\frac{\partial Q}{\partial \sigma_3} = -(1+\sin\varphi_0) + 2c_{90}\cos\varphi_0\left[q_1q_2(\sigma_2-\sigma_3)^{q_2-1} + \frac{1+\sin\varphi_0}{4\cos\varphi_0 c_{90}} + \sin\left(\omega-\frac{\pi}{4}\right)\cos\frac{\pi(\beta-\beta_{\max})}{\pi-2\beta_{\max}}\cdot q_3\right] \tag{21}$$

When $\beta = 90°$, $\sigma_2 = \sigma_3$, the plastic potential function has no β, ω and stress difference effect. The deformation pattern of the sample is the same as that of isotropic rock under conventional triaxial compression, i.e. $\frac{\partial Q}{\partial \sigma_2} = \frac{\partial Q}{\partial \sigma_3}$:

$$\frac{\partial Q}{\partial \sigma_2} = \frac{\partial Q}{\partial \sigma_3} = -\frac{1+\sin\varphi_0}{2} \tag{22}$$

When $\beta = 90°$, $\sigma_2 \neq \sigma_3$, the plastic potential function has no β, ω effect and has a stress-difference effect, in this case $\frac{\partial Q}{\partial \sigma_2}$ and $\frac{\partial Q}{\partial \sigma_3}$ are shown in Eqs. (23) and (24):

$$\frac{\partial Q}{\partial \sigma_2} = -2c_{90}\cos\varphi_0\left[q_1q_2(\sigma_2-\sigma_3)^{q_2-1} + \frac{1+\sin\varphi_0}{4\cos\varphi_0 c_{90}}\right] \tag{23}$$

$$\frac{\partial Q}{\partial \sigma_3} = -(1+\sin\varphi_0) + 2c_{90}\cos\varphi_0\left[q_1q_2(\sigma_2-\sigma_3)^{q_2-1} + \frac{1+\sin\varphi_0}{4\cos\varphi_0 c_{90}}\right] \tag{24}$$

where q_1 and q_2 represent the effect of the stress difference on the deformation of thin-layered rocks in the σ_2 and σ_3 directions and $q_1 < 0$, $q_2 > 1$. The variation patterns of $\frac{\partial Q}{\partial \sigma_2}$ and $\frac{\partial Q}{\partial \sigma_3}$ with σ_2 under different q_1 and q_2 values are shown in Fig. 15. It can be seen that the larger the absolute value of q_1 and q_2, the greater the influence of the stress difference on the deformation of thin-layered rocks. With the change in q_1, $\frac{\partial Q}{\partial \sigma_2}$ and $\frac{\partial Q}{\partial \sigma_3}$ show a linear trend, while with the change in q_2, $\frac{\partial Q}{\partial \sigma_2}$ and $\frac{\partial Q}{\partial \sigma_3}$ show a non-linear trend, as shown in Fig. 16; q_1 and q_2 can be identified by creep deformation data of samples under different β, ω, and b values.

When $\beta \neq 90°$, $\sigma_2 = \sigma_3$, the plastic potential function has no stress-difference effect but does have a β, ω-effect, in this case $\frac{\partial Q}{\partial \sigma_2}$ and $\frac{\partial Q}{\partial \sigma_3}$ are as given by Eqs. (25) and (26):

$$\frac{\partial Q}{\partial \sigma_2} = -2c_{90}\cos\varphi_0\left[\frac{1+\sin\varphi_0}{4\cos\varphi_0 c_{90}} + \sin\left(\omega-\frac{\pi}{4}\right)\cos\frac{\pi(\beta-\beta_{\max})}{\pi-2\beta_{\max}}\cdot q_3\right] \tag{25}$$

$$\frac{\partial Q}{\partial \sigma_3} = -(1+\sin\varphi_0) + 2c_{90}\cos\varphi_0\left[\frac{1+\sin\varphi_0}{4\cos\varphi_0 c_{90}} + \sin\left(\omega-\frac{\pi}{4}\right)\cos\frac{\pi(\beta-\beta_{\max})}{\pi-2\beta_{\max}}\cdot q_3\right] \tag{26}$$

where q_3 represents the effect of bedding structure on deformation of thin-layered rocks in the σ_2 and σ_3 directions and $0 < q_3 < \frac{1+\sin\varphi_0}{2\sqrt{2}\cos\varphi_0 c_{90}}$. The variation patterns of $\frac{\partial Q}{\partial \sigma_2}$ and $\frac{\partial Q}{\partial \sigma_3}$ with ω under different q_3 values at $\beta = 30°$ are shown in Fig. 17. It can be seen that the greater the value of q_3, the larger the influence of bedding structure on the deformation of thin-layered rocks. q_3 can be identified by creep deformation data pertaining to samples at a certain β value and different ω values under conventional triaxial compression.

When $\beta \neq 90°$, $\sigma_2 \neq \sigma_3$, the plastic potential function has β, ω, and stress difference effects, and $\frac{\partial Q}{\partial \sigma_2}$ and $\frac{\partial Q}{\partial \sigma_3}$ are as given by Eqs. (20) and (21).

Interestingly, the experimental results show that the fracture of siliceous slate always develops along a dominant direction under true triaxial creep loading. When the sample fails, the expansion deformation in one of the σ_2 or σ_3 direction is large, while that in

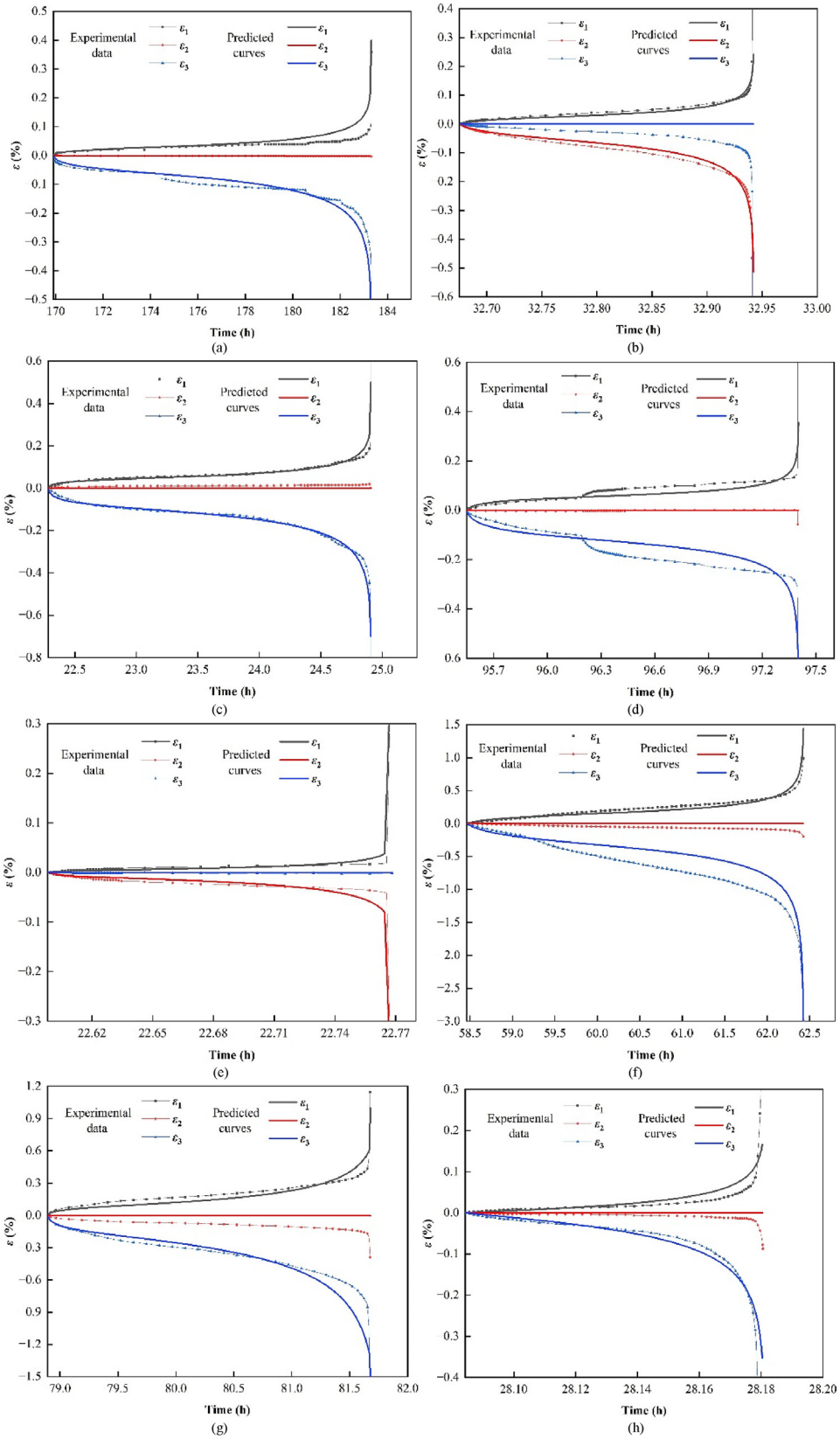


Fig. 19. Comparison between experimental and predicted results of creep strain of siliceous slate under true triaxial creep compression ($\sigma_3 = 3$ MPa): (a) $\beta = 0°$, $\omega = 0°$, $\sigma_2 = 10$ MPa, (b) $\beta = 0°$, $\omega = 90°$, $\sigma_2 = 10$ MPa, (c) $\beta = 0°$, $\omega = 0°$, $\sigma_2 = 50$ MPa, (d) $\beta = 30°$, $\omega = 0°$, $\sigma_2 = 10$ MPa, (e) $\beta = 30°$, $\omega = 90°$, $\sigma_2 = 10$ MPa, (f) $\beta = 30°$, $\omega = 90°$, $\sigma_2 = 30$ MPa, (g) $\beta = 30°$, $\omega = 90°$, $\sigma_2 = 50$ MPa, (h) $\beta = 45°$, $\omega = 0°$, $\sigma_2 = 20$ MPa, (i) $\beta = 60°$, $\omega = 90°$, $\sigma_2 = 10$ MPa, (j) $\beta = 75°$, $\omega = 0°$, $\sigma_2 = 10$ MPa, (k) $\beta = 75°$, $\omega = 0°$, $\sigma_2 = 15$ MPa, (l) $\beta = 90°$, $\sigma_2 = 5$ MPa, and (m) $\beta = 90°$, $\sigma_2 = 10$ MPa.

the other direction is small. That is, under different stress differences and loading angles, it is rare for both σ_2 and σ_3 directions to generate significant expansion simultaneously. This phenomenon may be related to the bedding structure and the uneven distribution of primary fractures within the siliceous slate. The plastic potential function proposed above, however, determines that the deformations of the specimen in the σ_2 and σ_3 directions are continuously changing, which is inconsistent with this phenomenon. Therefore, to enable the model to simulate different types of thin-layered rocks, another form of partial derivatives of the plastic potential function to the three principal stresses can be proposed as shown in Eqs. (27) and (28). The partial derivative forms in Eqs. (27) and (28) are suitable for thin-layered rock that fractured along a dominant direction under different stress differences and loading angles. While the partial derivative forms in Eqs. (19)–(21) are suitable for thin-layered rock that fractured in both σ_2 and σ_3 directions under some stress differences and loading angles conditions. Eqs. (27) and (28) are used herein to calculate the creep deformation of siliceous slate:

$$Sur = q_1 q_2 (\sigma_2 - \sigma_3)^{q_2 - 1} + \sin\left(\omega - \frac{\pi}{4}\right) \cos \frac{\pi(\beta - \beta_{\max})}{\pi - 2\beta_{\max}} \cdot q_3 \tag{27}$$

$$\begin{cases} \dfrac{\partial Q}{\partial \sigma_1} = 1 - \sin\varphi_0, \dfrac{\partial Q}{\partial \sigma_2} = 0, \dfrac{\partial Q}{\partial \sigma_3} = -(1 + \sin\varphi_0) \, (Sur < 0) \\ \dfrac{\partial Q}{\partial \sigma_1} = 1 - \sin\varphi_0, \dfrac{\partial Q}{\partial \sigma_2} = -(1 + \sin\varphi_0), \dfrac{\partial Q}{\partial \sigma_3} = 0 \, (Sur > 0) \end{cases} \tag{28}$$

where Sur is the interface where the dominant fracture orientation of thin-layered rock changes, when $Sur < 0$, the sample mainly expands in the σ_3 direction, when $Sur > 0$, the sample mainly expands in the σ_2 direction.

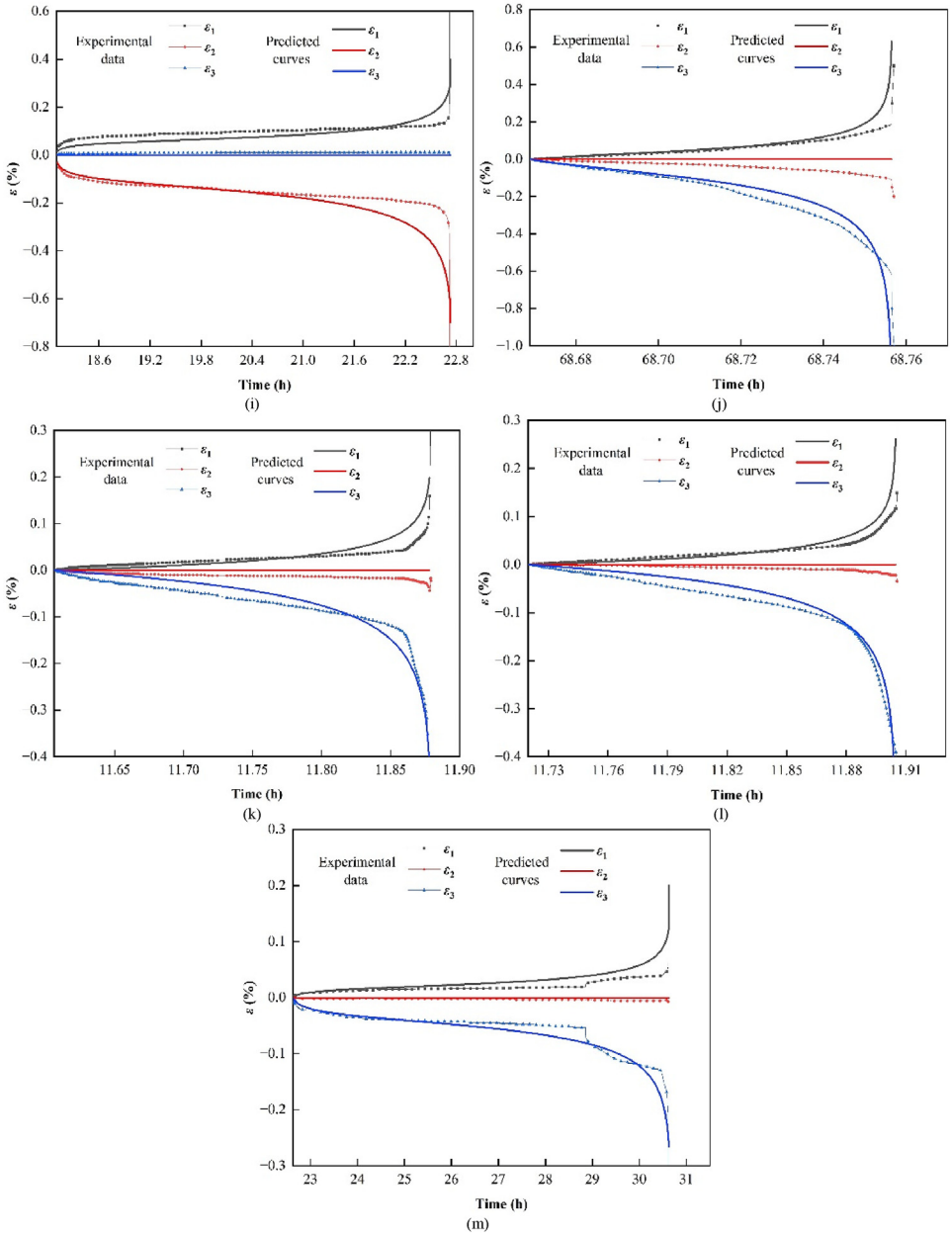


Fig. 19. (*continued*).

4.2. Verification of the 3D anisotropic creep model for thin-layered rocks

Due to the fact that the long-term strength and creep deformation characterization of thin-layered rocks under true triaxial stress conditions involves many factors, more parameters are required compared to the number needed to model quasi-isotropic rocks. Therefore, the form of creep model for thin-layered rocks is more complex, and the identification of these parameters requires a lot of experiments; however, the cost of a large number of true triaxial tests is relatively high, and due to the significant discreteness of thin-layered rocks, it is difficult to ensure homogeneity of the samples. Based on this, non-linear fitting methods were used to identify the model parameters of siliceous slate, and the results are shown in Tables 4 and 5. The prediction results of the proposed creep model for long-term strength and 3D creep deformation of rock samples are calculated through MATLAB™ programming.

Comparisons of measured and predicted data pertaining to the long-term strength and creep deformation in three principal stress directions of siliceous slate are shown in Figs. 18 and 19. This paper mainly explored the creep fracture behavior of thin-layered rocks, which mainly occurs during the last level of creep loading, therefore, the creep deformation of the last level of creep loading was calculated. Fig. 18a shows that the predicted long-term strength surfaces of the proposed model can reflect the β-related effect, ω-related strengthening effect and intermediate principal stress strengthening effect of thin-layered rock long-term strength. Fig. 18b shows that the predicted long-term strength values are consistent with the creep test data under true triaxial compression. The strength data are concentrated near the reference line ($\sigma_{1\mathrm{pred}} = \sigma_{1\mathrm{exp}}$), and most data points are distributed within the ±15% error lines. The average relative error (Eq. (29)) between the predicted values and experimental values is 6.44%:

$$\overline{\delta} = \frac{1}{x}\sum_{i=1}^{x}\left|\frac{\sigma_{1\ \exp(i)} - \sigma_{1\mathrm{pred}(i)}}{\sigma_{1\ \exp(i)}}\right|, x = 1, 2, 3\ldots \tag{29}$$

where $\overline{\delta}$ is the average relative error; $\sigma_{1\exp(i)}$ denotes the experimental data; and $\sigma_{1\mathrm{pred}(i)}$ refers to the predicted data.

Fig. 19 shows that the predicted creep deformation curves in three principal stress directions of siliceous slate are consistent with the creep test data under true triaxial compression. It should be noted that in addition to parameters λ_1 and λ_2, one set of parameters can be used to simulate the long-term strength and creep deformation of siliceous slate under different loading angles and stress states. The differences in parameters λ_1 and λ_2 for each rock sample are caused by the high discreteness of the thin-layered rock specimens. These results indicate that the 3D anisotropic nonlinear creep model proposed herein can reflect the anisotropic long-term strength, anisotropic failure process, anisotropic fracture orientation, and three creep-deformation stages of thin-layered rocks under different loading angles and stress differences with one set of parameters.

5. Discussion

This paper conducted a series of true triaxial creep compression tests on typical thin-layered rock siliceous slate and constructed a 3D creep model to reveal and simulate its anisotropic time-dependent fracture characteristics. However, due to the restrictions of the experimental conditions or other factors, several aspects require optimization and improvement:

(1) This article simulated the anisotropic long-term strength and 3D creep deformation of the samples, but did not simulate the complex creep failure mode of thin-layered rock under true triaxial compression conditions, which needs to be addressed in future studies. The engineering scale simulation of the time-dependent failure of thin-layered rock tunnel should also be conducted in the future.
(2) Further research should be conducted on the creep failure characteristics of thin-layered rocks when the intermediate principal stress approaches the maximum principal stress (the stress state parameter $b > 0.5$) in the future.
(3) When the stress effect is in competition with the structure effect and the stress plays a dominant role in the failure of the specimen, the samples exhibit significant plastic deformation before macroscopic failure occurs (Fig. 9f–g). The above phenomenon may be due to the intense competition for microcrack propagation in different directions before a macroscopic fracture surface is formed. Systematic experiments and theoretical analysis should be carried out to explain this phenomenon in future studies.
(4) The applicability of the model proposed in this article to different types of thin-layered rocks at different time scales needs further research.

6. Conclusions

Based on true triaxial creep compression tests and AE monitoring technology, the anisotropic long-term strength, creep deformation, and fracture characteristics of thin-layered rock are systematically studied under the coupling effect of inherent anisotropy and intermediate principal stress. Based on the experimental results, a 3D creep model of thin-layered rocks was constructed, and the model was validated based on experimental results. The main conclusions are as follows:

(1) The creep failure mode of thin-layered rocks is jointly controlled by stress and bedding structure. When the loading angles and stress difference are small, the creep failure mode of the sample is mainly controlled by the bedding structure, otherwise, it is mainly controlled by stress. When shear-slip fracture occurs along the bedding plane, the rock specimens exhibit sudden failure characteristics; when mixed tensile-shear fractures propagate through the bedding planes, rock specimens exhibit relatively progressive failure characteristics; when mixed tensile fractures are generated along the bedding planes and shear fractures propagate through the bedding planes, the specimens exhibit progressive failure characteristics;
(2) The creep fracture orientations of thin-layered rocks are jointly controlled by stress and bedding structure. Thin-layered rocks always tend to expand along the σ_3 direction and the normal direction of bedding plane. When ω is small, the effects of stress and structure are combined, the deformation in the σ_3 direction is large. When ω is large, the stress effect is in competition with the structure effect, if the stress difference is small, the bedding structure plays a dominant role in the failure of the specimen, and the deformation in the σ_2 direction is relatively large, if the stress difference is large, the stress plays a dominant role, and the deformation in the σ_3 direction is relatively large;
(3) A 3D anisotropic non-linear creep model for thin-layered rock is derived based on overstress theory and a true

triaxial failure criterion for anisotropic rock. The time-dependent fracture process of rocks during true triaxial creep loading is reflected through the change of equivalent strain based on improved Euler iteration method. By constructing the plastic potential function and overstress index related to loading angles and stress differences, the anisotropic time-dependent fracturing process and fracture orientation of thin-layered rocks under different loading angles and stress differences can be reflected by the model;

(4) The test results indicate that the predicted long-term strength and creep deformation are consistent with the creep test data of siliceous slate under true triaxial compression. Therefore, the 3D anisotropic nonlinear creep model proposed in this paper can characterize the anisotropic long-term strength, anisotropic fracture process, anisotropic fracture orientation and three creep deformation stages of thin-layered rocks under different loading angles and stress differences with one set of parameters.

Declaration of competing interest

The authors declare that they have no known competing financial interests or personal relationships that could have appeared to influence the work reported in this paper.

Acknowledgments

The authors acknowledge the financial support from the 111 Project (Grant No. B17009) and the Liao Ning Revitalization Talents Program (Grant No. XLYCYSZX1902). The authors also thank Dr. Xufeng Liu at Institute of Rock and Soil Mechanics, Chinese Academy of Sciences, China, for his assistance in paper revision.

List of symbols

β, ω	True triaxial loading angles for thin-layered rock samples
θ	Angle between the direction of wave propagation and the bedding plane
$\dot{\varepsilon}_{ij}$, $\dot{\varepsilon}_{ij}^{e}$, $\dot{\varepsilon}_{ij}^{vp}$	Total, elastic and visco-plastic strain rate tensor, respectively
$\dot{\sigma}_{ij}$	Stress rate tensor
D_{ij}	Elastic compliance matrix
F_0	Long-term strength of specimen
σ_1, σ_2, σ_3	Maximum, intermediate, and minimum principal stresses, respectively
ε_1, ε_2, ε_3	Principal strains corresponding to three principal stresses, respectively
$\bar{\varepsilon}^{p}$, $\bar{\varepsilon}_0^{p}$, $\bar{\varepsilon}_e^{p}$	Equivalent strain, equivalent strain at initial loading and equivalent strain at the end of loading, respectively
λ	Viscosity parameter
λ_1, λ_2	Two visco-plastic flow coefficients
a	Attenuation coefficient of the visco-plastic flow coefficient
b	A parameter describing the stress state
φ_b, φ_0	Friction angle with different b and friction angle at $b = 0$, respectively
$c_{\beta\omega b}$, c_{90}	Cohesion with different β, ω, b and cohesion at $\beta = 90°$, respectively
β_{min}	Angle corresponding to the lowest strength under conventional triaxial compression
β_{max}	Angle corresponding to the most affected by ω under true triaxial compression
s, t, A, n, D, m	Parameters in the true triaxial failure criterion for anisotropic rock
I	Time-dependent fracture coefficient
N	Overstress index
d_1	Parameter mainly affecting N at $\beta = \omega = 0°$
d_2	Parameter mainly affecting the degree of influences of ω and b on N
d_3	Parameter mainly affecting N at $\beta = 90°$
q_1, q_2	Two parameters affecting the degree of influences of the stress difference on the deformation of thin-layered rocks, respectively
q_3	Parameter affecting the degree of influences of the bedding structure on deformation of thin-layered rocks

References

Choo, J., Semnani, S.J., White, J.A., 2021. An anisotropic viscoplasticity model for shale based on layered microstructure homogenization. Int. J. Numer. Anal. Methods GeoMech. 45 (4), 502–520.
Deng, H., Wang, W., Li, J., Zhang, Y., Zhang, X., 2018. Experimental study on anisotropic characteristics of bedded sandstone. Chin. J. Rock Mech. Eng. 37 (1), 112–120.
Feng, X., Kong, R., Yang, C., Zhang, X., Wang, Z., Han, Q., Wang, G., 2020. A three-dimensional failure criterion for hard rocks under true triaxial compression. Rock Mech. Rock Eng. 53 (1), 103–111.
Feng, X., Yu, X., Zhou, Y., Yang, C., Wang, F., 2023. A rigid true triaxial apparatus for analyses of deformation and failure features of deep weak rock under excavation stress paths. J. Rock Mech. Geotech. Eng. 15 (5), 1065–1075.
Guo, J., Yang, J., Chen, W., Shen, D., Liu, T., Chai, W., 2019. Research on large deformation of surrounding rock and mechanical characteristics of lining of carbonaceous slate tunnel based on field measurement. Chin. J. Rock Mech. Eng. 38 (4), 832–841.
Huang, X., Liu, Q., Bo, Y., Liu, B., Ding, Z., Zhang, Q., 2022. An elasto-plastic and viscoplastic damage constitutive model for dilatancy and fracturing behavior of soft rock squeezing deformation. J. Mt. Sci. 19 (3), 826–848.
Ismael, M., Imam, H., El-Shayeb, Y., 2014. A simplified approach to directly consider intact rock anisotropy in Hoek–Brown failure criterion. J. Rock Mech. Geotech. Eng. 6, 486–492.
Ismael, M., Konietzky, H., Imam, H., Helal, H., 2015. Extension and modification of Hoek and Brown failure criterion to incorporate anisotropy. In: Schubert, Kluckner (Ed.), EUROCK 2015 & 64th Geomechanics Colloquium. ÖGG, Salzburg, pp. 767–772.
Ismael, M., Konietzky, H., 2017. Integration of elastic stiffness anisotropy into ubiquitous joint model. Procedia Eng. 191, 1032–1039.
Ismael, M., Konietzky, H., Herbst, M., 2019. A new continuum-based constitutive model for the simulation of the inherent anisotropy of Opalinus clay. Tunn. Undergr. Space Technol. 93, 103106.
Ismael, M., Konietzky, H., 2019. Constitutive model for inherent anisotropic rocks: ubiquitous joint model based on the Hoek-Brown failure criterion. Comput. Geotech. 105, 99–109.
Kou, H., He, C., Yang, W., Wu, F., Zhao, Z., Fu, J., Xiao, L., 2023. A fractional nonlinear creep damage model for transversely isotropic rock. Rock Mech. Rock Eng. 56 (2), 831–846.
Liang, C., Li, X., Li, S., Hao, J., Ma, C., 2012. Study of strain stress threshold value between static loading and quasi-dynamic loading of rock. Chin. J. Rock Mech. Eng. 31 (6), 1156–1161.
Liu, G., Zhang, F., Li, X., Yang, Z., 2005. Research on large deformation and its mechanism of Muzhailing tunnel. Chin. J. Rock Mech. Eng. 24 (S2), 5521–5526.
Liu, X., Feng, X., Zhou, Y., 2020. Experimental study of mechanical behavior of gneiss considering the orientation of schistosity under true triaxial compression. Int. J. GeoMech. 20 (11), 04020199.
Liu, X., Feng, X., Zhou, Y., Sharifzadeh, M., 2022. Influences of foliation orientation and lateral stress difference on the deformation and fracturing of a thin-layered rock around underground excavations: insight from multi-axial loading tests. Bull. Eng. Geol. Environ. 81 (5), 171.
Liu, X., Feng, X., Zhou, Y., 2023. Influences of schistosity structure and differential stress on failure and strength behaviors of an anisotropic foliated rock under true triaxial compression. Rock Mech. Rock Eng. 56 (2), 1273–1287.
Liu, Z., Xie, S., Shao, J., Conil, N., 2015. Effects of deviatoric stress and structural anisotropy on compressive creep behavior of a clayey rock. Appl. Clay Sci. 114, 491–496.
Mogi, K., 2006. Experimental Rock Mechanics. Taylor and Francis, London, U.K.
Ohno, K., Ohtsu, M., 2010. Crack classification in concrete based on acoustic emission. Construct. Build. Mater. 24, 2339–2346.
Pietruszczak, S., Lydzba, D., Shao, J., 2004. Description of creep in inherently anisotropic frictional materials. J. Eng. Mech. 130 (6), 681–690.
Rassouli, F.S., Zoback, M.D., 2018. Comparison of short-term and long-term creep experiments in shales and carbonates from unconventional gas reservoirs. Rock

Mech. Rock Eng. 51 (7), 1995–2014.
Sone, H., Zoback, M.D., 2014. Time-dependent deformation of shale gas reservoir rocks and its long-term effect on the in situ state of stress. Int. J. Rock Mech. Min. Sci. 69, 120–132.
Song, T., Zhou, Y., Yu, X., 2024. Three-dimensional acoustic emission source localization method for layered rock considering anisotropic P-wave velocity. Bull. Eng. Geol. Environ. 83, 185.
Tian, Y., Chen, W., Tian, H., Yang, J., Zhang, Z., Shu, X., 2021. Analytical model of layered rock considering its time-dependent behaviour. Rock Mech. Rock Eng. 54 (11), 5937–5944.
Wang, Z., Zong, Z., Qiao, L., Li, W., 2018. Transversely isotropic creep model for rocks. Int. J. GeoMech. 18 (6), 04018033.
Xu, G., He, C., Chen, Z., Su, A., 2018a. Transverse isotropy of phyllite under Brazilian tests: laboratory testing and numerical simulations. Rock Mech. Rock Eng. 51 (4), 1111–1135.
Xu, G., He, C., Su, A., Chen, Z., 2018b. Experimental investigation of the anisotropic mechanical behavior of phyllite under triaxial compression. Int. J. Rock Mech. Min. Sci. 104, 100–112.
Xu, G., He, C., Yan, J., Ma, G., 2019. A new transversely isotropic nonlinear creep model for layered phyllite and its application. Bull. Eng. Geol. Environ. 78 (7), 5387–5408.
Xu, G., He, C., Chen, Z., Yang, Q., 2020. Transversely isotropic creep behavior of phyllite and its influence on the long-term safety of the secondary lining of tunnels. Eng. Geol. 278, 105834.
Yan, B., Guo, Q., Ren, F., Cai, M., 2020. Modified Nishihara model and experimental verification of deep rock mass under the water-rock interaction. Int. J. Rock Mech. Min. Sci. 128, 104250.
Zhang, X., Wong, L.N.Y., Wang, S., Han, G., 2011. Engineering properties of quartz mica schist. Eng. Geol. 121 (3–4), 135–149.
Zhao, J., Feng, X., Zhang, X., Yang, C., Zhou, Y., 2018. Time-dependent behaviour and modeling of Jinping marble under true triaxial compression. Int. J. Rock Mech. Min. Sci. 110, 218–230.
Zhou, H., Wang, C., Han, B., Duan, Z., 2011. A creep constitutive model for salt rock based on fractional derivatives. Int. J. Rock Mech. Min. Sci. 48 (1), 116–121.
Zhou, Y., Feng, X., Xu, D., Fan, Q., 2016. Experimental investigation of the mechanical behavior of bedded rocks and its implication for high sidewall caverns. Rock Mech. Rock Eng. 49 (9), 3643–3669.



Prof. Xia-Ting Feng received his PhD degree at Northeastern University of Technology (now Northeastern University since 1993), China in 1992 and then took the position of lecturer, associate professor and professor at the same university. He joined Institute of Rock and Soil Mechanics, Chinese Academy of Sciences (CAS) in 1998 as a Professor of Hundred Talent Program of the CAS and as Deputy Director in Charge and Director in 2001–2005. He has worked as Director of State Key Laboratory of Geomechanics and Geotechnical Engineering since 2007. He works at Northeastern University, China as a Vice President since September 2017. In February 2021, he became president of Northeastern University. He is President of Federation of International Geo - engineering Societies - FedIGS, President of International Society for Rock Mechanics (ISRM) Commission on Design Methodology, member of ISRM Commission on Testing Methods, and President of Chinese Society for Rock Mechanics and Engineering (CSRME). He was the past President of ISRM 2011–2015. He is also Editor-in-Chief of *Journal of Rock Mechanics and Geotechnical Engineering* (JRMGE), and Associate Editor-in-Chief of *Chinese Journal of Theoretical and Applied Mechanics*. He is member of Editorial Board of *Rock Mechanics and Rock Engineering*. His research interests cover rock mechanics for deep rock engineering. He published more than 180 technical papers and the English books "*Rock engineering design*" and "*Rock engineering risk*" with Professor John Hudson. He has edited five volumes of the book "*Rock mechanics and rock engineering*" (CRC Press) and the book "*Rockburst*" (Elsevier).